Stability and photometric accuracy of CMOS image sensors in space: Radiation damage, surface charge and quantum confinement in silicon detectors

Michael E. Hoenk

Jet Propulsion Laboratory, California Institute of Technology, Pasadena, CA 91109[1]

Stability and photometric accuracy of silicon imaging detectors are essential for the Habitable Worlds Observatory and a range of NASA missions that will explore time domain astrophysics and astronomy over a spectral range spanning soft X-rays through the ultraviolet (UV), visible, and near infrared. Detector stability is one of the oldest and most challenging problems in NASA missions. The challenges are particularly acute in the extreme ultraviolet range, where near-surface absorption of high-energy photons causes surfaces to degrade rapidly. The susceptibility of back-illuminated silicon detectors to ionizing radiation damage is dramatically demonstrated by the Extreme Ultraviolet Imaging Telescope (EIT) currently flying on the joint ESA-NASA Solar and Heliospheric Observatory (SOHO). Soon after launch, the Tektronix TK512CB CCD on EIT suffered severe degradation of charge collection efficiency caused by exposure to solar EUV radiation, resulting in (non)flat-field images with burned-in images of the sun. This had major consequences for the EIT consortium, which needed five years to develop a usable calibration method for the EUV-damaged detector.[1] In the quarter century after EIT's experience with calibrating radiation-damaged CCDs, considerable effort has gone into improving the stability and radiation-hardness of ion-implanted CMOS and CCD imaging arrays.[2] Despite significant improvements to the process, recent observations of quantum efficiency hysteresis (QEH) in Teledyne e2v (Te2v) CCDs raise important questions about the stability of back-illuminated silicon detectors.[3] In this paper, the effects of radiation-induced variability of surface charge on detector stability and photometric accuracy are analyzed in order to assess the implications for future NASA missions.

Before proceeding, we note that consultation with Teledyne-e2v revealed that the ion-implanted detectors tested in Heymes *et al.* are not representative of current device capabilities, and more recent devices are expected to have improved stability. Calculations using the model developed here show that increasing the surface dopant density will improve detector stability. Further study is needed to validate these results with more representative devices. JPL and Teledyne e2v are collaborating on the development and qualification of high-performance UV detectors for spaceflight.[4,5,6]

QE data reported by Heymes *et al.* are reproduced in Figures 1 and 2, together with calculated QE from the model described below. Figure 1 shows the measured QE of a UV-enhanced CCD over the EUV-UV spectral range. Figure 2 shows the QE of the same device measured before and after prolonged exposure to 200nm photons. Data in the figures are compared with a QE model that I developed for this study as a generalization and expansion of the model used in our previous paper.[6] To accommodate arbitrary surface dopant profiles, the detector is divided into N regions and the boundary value problem is solved numerically using matrix calculations. Degenerate doping is addressed using bandgap narrowing data from Swirhun *et al.*,[7] which blunts strongly-peaked surface dopant profiles by reducing

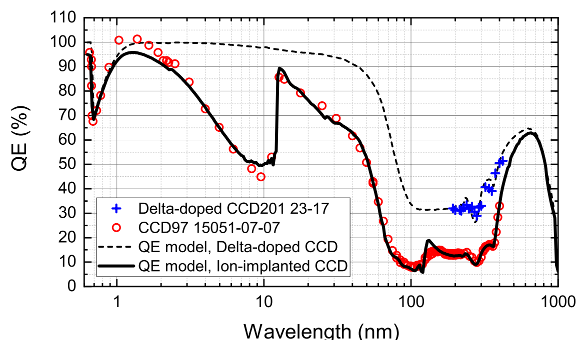

Figure 1: Quantum efficiency data for a UV-enhanced CCD97 detector are compared with calculated QE of an ion-implanted detector using trap densities $N_{it} = 3.45\text{x}10^{12}$ cm^{-2} and $N_{ot} = 10^{12}$ cm^{-2} as fitting parameters. The QE of a delta-doped CCD is shown for comparison.[6]

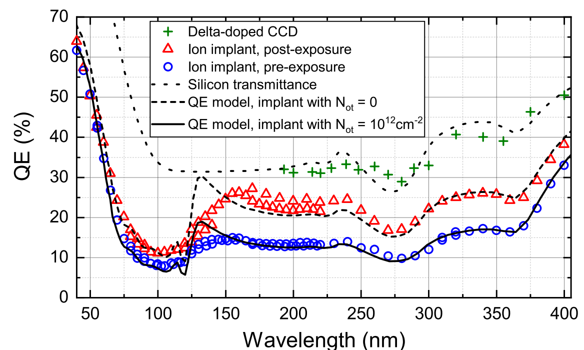

Figure 2: QE measurements of the CCD in Figure 1 before and after prolonged UV illumination show a persistent increase in QE caused by exposure to 200nm light.[3] The model shows the measured changes in response are consistent with UV-induced neutralization of positive charge trapped in the oxide.

[1] Corresponding author: Email: michael.e.hoenk@jpl.nasa.gov, Tel: 818-354-1881

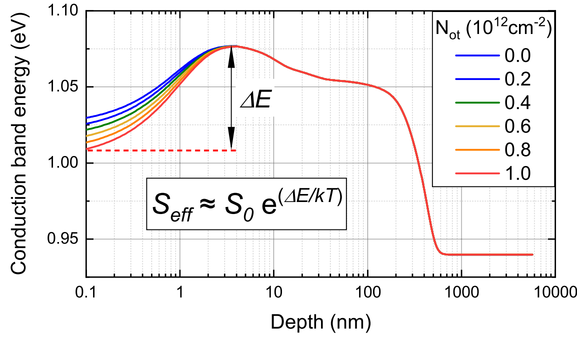

Figure 3: The backside potential well of the detector in Figure 1 (N_{it} = 3.45x10^{12}cm^{-2}) deepens as the density of charge trapped in the oxide (N_{ot}) varies from 0 to 10^{12}cm^{-2}. Because the *effective* surface recombination velocity (S_{eff}) varies exponentially with well depth, small variations in oxide charge can have a large effect on detector QE.

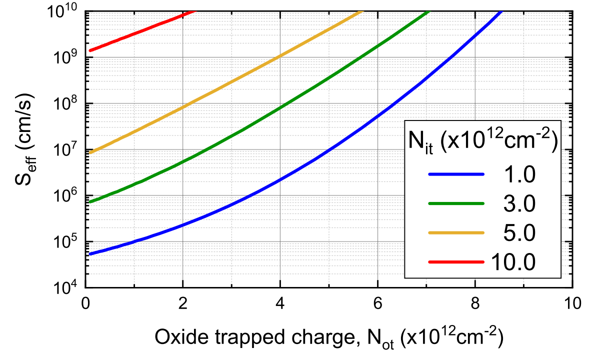

Figure 4: Exposure to ionizing radiation causes the Si-SiO_2 interface trap density (N_{it}) to increase over time. At a given N_{it}, the effective surface recombination velocity (S_{eff}) varies roughly exponentially with oxide charge (N_{ot}). For comparison, see plots of internal quantum efficiency *vs* oxide trapped charge in Figures 5 and 6.

the potential barrier height and electric field strength near the surface. Finally, calculations of surface recombination velocity in terms of interface and oxide trap densities are based on Shockley-Read-Hall (SRH) statistics applied to semiconductor surfaces, using formulae derived in Andrew Grove's 1967 book on semiconductor physics,[8] and further developed and refined in models of solar cell performance to include an integration over the silicon bandgap.[9] To accomplish this, the model incorporates measurements of cross sections and densities of states *vs* energy for Pb_0 traps at the Si-SiO_2 interface.[10] Poisson's equation is solved self-consistently to calculate the surface potential as a function of the densities of interface traps (N_{it}) and oxide charge (N_{ot}). Grove's introduction of an effective surface recombination velocity (S_{eff}) is useful as a heuristic explanation of QE instabilities caused by variable oxide charge in radiation-damaged detectors (see Figures 3 and 4). For this study, I've used the more exact formulae for SRH surface recombination in order to investigate the two main sources of surface charge in detectors, interface and oxide traps (N_{it} and N_{ot}), which are conflated in models relying on S_{eff}. Radiation-induced variability in the occupation of oxide traps is essential for the interpretation of QEH data in Heymes *et al.* and for the following analysis of radiation damage and detector stability in space.

The data in Figure 2 are characteristic of QEH instability, which Jim Janesick described in 1989 as having "plagued the back-illuminated CCD since its invention."[11] The discovery of QEH in state-of-the-art ion-implanted CCDs presents problems and challenges that are important for time domain astronomy. Strategies for the mitigation of QEH instabilities involve flooding the detector with light to charge the detector surface and thereby stabilize the response. In 2013, European Southern Observatory (ESO) astronomers reported that Janesick's UV flood process could be used in ground-based telescopes to improve the UV QE of ion-implanted detectors by up to 50%.[12] In 2010, observations of QEH in Wide Field Camera 3 (WFC3) CCDs motivated the development of a "pinning exposure" that was performed periodically on orbit to neutralize a 4% QE deficit observed after each annealing cycle.[13]

Despite their similarities, the UV flood processes used by ESO astronomers, WFC3, and Heymes *et al.* employ different surface charging mechanisms. Janesick's UV flood process charges the surface while the detector is warm by catalyzing the chemisorption of negatively charged O_2 ions on the oxide surface, whereas Heymes *et al.* charged the surface while the detector was cold and under vacuum. In the absence of oxygen, what is causing surface charge to change in Heymes' UV-flood experiment? The answer to this question can be found in a classic experiment performed at Caltech by Carver Mead in 1967, as reported by Snow, Grove and Fitzgerald, which demonstrates UV-induced neutralization of radiation-induced oxide space charge with a threshold photon energy of 4.0 to 5.0 eV.[14]

Based on data and models of radiation-induced degradation of Si-SiO_2 interfaces in MOS devices, I propose that the QEH measured by Heymes *et al.* was caused by UV-induced charge injection, which saturates when positive charge trapped in the oxide is neutralized (see Figure 2). In experimental studies of trap-generation dynamics in MOS structures, Nissan-Cohen *et al.* proposed a dynamic charging model based on the idea that oxide charge reaches a steady-state trapping level that depends on the electric field in the oxide.[15] Saturation of QEH in experiments performed by Heymes *et al.* can thus be

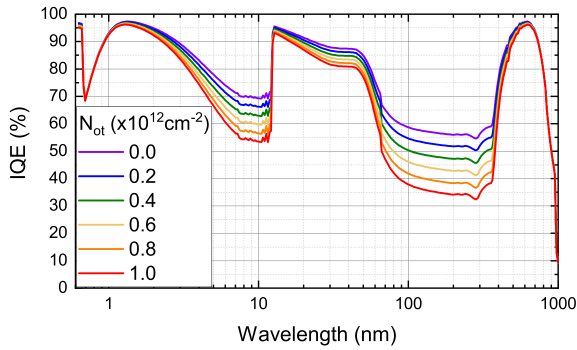

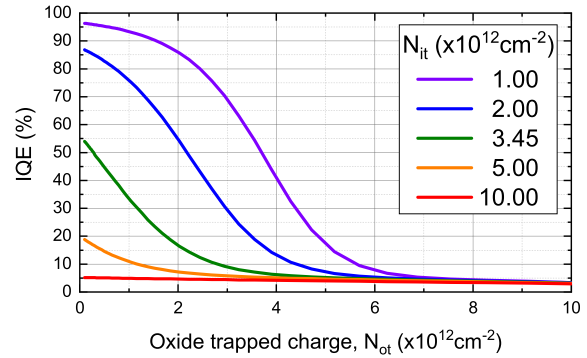

Figure 5: The internal quantum efficiency (IQE) of the detector in Figures 1 and 2 ($N_{it} \sim 3.45 \times 10^{12} cm^{-2}$) is very sensitive to variability of charge trapped in the oxide in time and space (N_{ot}). For comparison, the quantum efficiency hysteresis (QEH) measured by Heymes *et al.* corresponds to a change in N_{ot} of approximately 10^{12} cm^{-2}.

Figure 6: Radiation-induced degradation of IQE at 285nm is depicted here in terms of interface and oxide trapped charge. At the beginning of life, the UV QE is high because of low N_{it}. Exposure to ionizing radiation damages the oxide, leading to degradation of QE and increased susceptibility QEH (UV-induced variability of oxide charge).

understood in terms of an equilibrium charge density formed in the oxide.[3] Experimental studies of vacuum ultraviolet (VUV) induced radiation damage in MOS oxides reported by Afanas'ev *et al.* showed that whereas charge injection into thermal SiO_2 is initially slow because of the small cross section of traps in high-quality thermal oxides, ionizing radiation causes accelerated rates of charging and degradation due to "positive feedback in the generation of oxygen vacancies and the clustering of defects, which appear to take place in the degeneration of the MOS system upon VUV irradiation."[16]

Data and models describing radiation-induced charge injection in MOS oxides, together with calculations using the QE model described in this paper, suggest a causal relationship between radiation damage, oxide charge, and quantum efficiency hysteresis in ion-implanted CCDs. Figure 5 analyzes the spectral response of detectors with different oxide charge densities, using the dopant profile and interface trap density derived for the Heymes *et al.* CCD (Figure 1). As expected, the greatest variability in internal quantum efficiency (IQE) occurs in the ultraviolet where absorption takes place near the surface, but significant changes are seen across the entire spectral range measured by Heymes *et al.* Figure 6 extends this analysis by calculating QEH at a specific wavelength (285nm) as a function of interface and oxide trap densities. These calculations show that measurable QEH may exist even at the beginning of life, while Heymes *et al.* (Figure 2) showed that UV-induced surface charge can increase QE by a factor of up to 1.6 at 285nm.[3] The implications for NASA missions can be appreciated in light of the consequences of EUV-induced radiation damage on the calibration of SOHO EIT CCDs.[1]

Radiation-induced charge injection and structural damage to surface dielectrics on silicon have important consequences for field-effect passivation of silicon detectors, which includes surface charging methods such as flash gates, chemisorption, and charged dielectrics (*e.g.*, Al_2O_3, SiN_x, and high-κ dielectrics, which are used in solar cells and commercial CMOS imaging detectors). In 2007, MIT Lincoln Labs published a study on CCDs for the EUV Variability Experiment, which showed that ion implantation and MBE-grown silicon are far more radiation-hard than chemisorption passivation.[17]

The QE of a delta-doped detector is plotted in Figure 7 in comparison with calculated QE for a delta-doped detector with an interface trap density of $10^{14}cm^{-2}$ and oxide trap densities varying from 10^{13} to $10^{14}cm^{-2}$. Despite the fact that these levels of surface are two orders of magnitude larger than those calculate for the Heymes *et al.* CCD, the model shows that the QE of a delta-doped detectors is remarkably stable. The tolerance of delta-doped detectors to such extreme levels of radiation damage is explained in Figure 8, which shows that the surface depletion layer is effectively pinned at the position of the first delta layer, independent of variability of interface and oxide trapped charge. Wheres the model predicts residual losses associated with absorption in MBE silicon, data in Figure 7 show that delta-doped detectors respond with nearly 100% internal QE. This discrepancy is attributed to quantum effects in the delta-doped surface, which are not included in the model.[18] In 2012 and 2013, Alacron and Applied Materials verified the near-100% QE and radiation-hardness of delta-doped CMOS detectors in months-long accelerated lifetime tests using pulsed excimer lasers at 193nm and 263nm.[18]

Using molecular beam epitaxy (MBE), JPL has developed multilayer 2D-doping to increase surface conductivity (important for high-speed CMOS imaging detectors), compensate defects at the MBE-

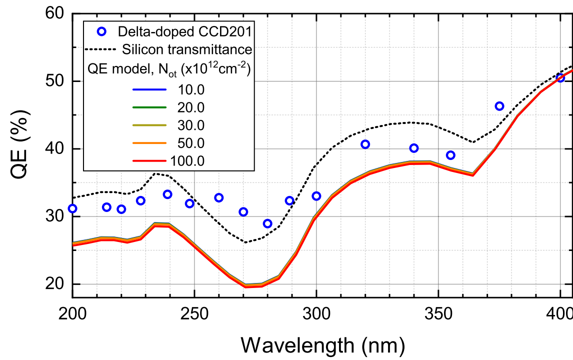

Figure 7: The calculated QE of a delta-doped detector is stable against interface trap densities up to 10^{14}cm^{-2}, in agreement with experiment. QE data for a delta-doped CCD201 are plotted for comparison.[6] The discrepancy between the QE model and silicon transmittance is attributed to quantum effects, which are not in the model.

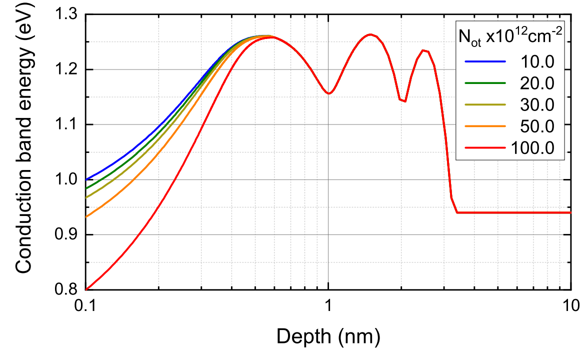

Figure 8: The conduction band edge of a delta-doped detector is shown here for oxide charge densities in the range of 10^{13} - 10^{14}cm^{-2}. The 2D-dopant profile achieve by MBE growth effectively pins the surface depletion layer at the location of the first delta layer. On these length scales, quantum effects dominate carrier transport phenomena.

detector interface, and enhance the stability of delta-doped detectors in high radiation environments. The atomic scale control required to realize these capabilities is the exclusive domain of molecular beam epitaxy and atomic layer deposition technologies developed at JPL's Microdevices Laboratory.[19]

Acknowledgements

This work would not have been possible without the exceptional work of scientists in JPL's Advanced UV detectors team: Shouleh Nikzad, April Jewell, John Hennessy, Todd Jones, Gillian Kyne, Chaz Shapiro, and Nathan Bush. I would like to thank David Morris for providing Teledyne e2v's ion implantation profile and for many valuable discussions. The research described in this paper was carried out at the Jet Propulsion Laboratory, California Institute of Technology, under a contract with the National Aeronautics and Space Administration.

References

[1] Clette *et al.* 2002, "The Radiometric Calibration of the Extreme Ultraviolet Imaging Telescope," *The Radiometric Calibration of SOHO (ESA SR-002)*, Edited by A. Pauluhn, M.C.E. Huber and R. von Steiger.
[2] Jerram *et al.* 2010, "Back-thinned CMOS sensor optimization," *Proc. SPIE* 7598, 759813
[3] Heymes *et al.*, 2020, "Comparison of back-thinned detector ultraviolet quantum efficiency for two commercially available passivation treatments," *IEEE Transactions on Nuclear Science*, 67(8), 1962-1967
[4] Kyne *et al.* 2020, "Delta-doped electron-multiplying CCDs for FIREBall-2," *JATIS* 6(1), 011007
[5] Jewell *et al.* 2018, "Ultraviolet detectors for astrophysics missions: a case study with the star-planet activity research cubesat (SPARC)," *Proc. SPIE 10709,* 107090C
[6] Hoenk *et al.* 2022, "2D-doped silicon detectors for UV/optical/NIR and X-ray astronomy," *SPIE* 12191
[7] Swirhun *et al.* 1986, "Measurement of electron lifetime, electron mobility, and band-gap narrowing in heavily doped p-type silicon," *1986 International Electron Devices Meeting*, Los Angeles, CA, USA, 1986
Swirhun *et al.* 1987, "Temperature dependence of minority carrier electron mobility and bandgap narrowing in p+ silicon," *IEEE Trans. on Electron Dev.* ED-34(11): 2385.
[8] Grove 1967, *Physics and Technology of Semiconductor Devices,* John Wiley and Sons, New York;
[9] McIntosh *et al.* 2014, "On effective surface recombination parameters," *J. Appl. Phys.* 116, 014503
[10] Ragnarrson and Lundgren, 2000, "Electrical characterization of centers in (100) Si-SiO_2 structures: The influence of surface potential on passivation during post metallization anneal," *J. Appl. Phys.* **88**, 938
[11] Janesick *et al.*, 1989, "Charge-coupled device pinning technologies," *Proc. SPIE* 1071, 153-169.
[12] Deiries *et al.*, "Precision UV QE measurements of Optical Detectors with a special calibrated work bench," *Scientific Detector Workshop*, Florence, Italy, Oct 7–11, 2013.
[13] Baggett *et al.*, 2010, "WFC3 detectors: On-orbit performance," *Proc. SPIE* 7731, 773138.
[14] Snow et al., 1967, "Effects of ionizing radiation on oxidized silicon surfaces and planar devices," *Proc. IEEE*, 55(7): 1168-1185.
[15] Nissan-Cohen *et al.*, 1986, "Trap generation and occupation dynamics in SiO_2 under charge injection stress," *J. Appl. Phys.* **60**(6): 2024-2035.
[16] Afanas'ev *et al.*, "Degradation of the thermal oxide of the Si/SiO_2/Al system due to vacuum ultraviolet radiation," *J. Appl. Phys.* **78**(11): 6481-6490, 1995.
[17] Westhoff et al. 2007, "Radiation-hard, charge-coupled devices for the extreme ultraviolet variability experiment," *Proc. SPIE* 6686
[18] Hoenk *et al.* 2015, "Superlattice-doped imaging detectors: progress and prospects," *SPIE Proc.* 9154, High Energy, Optical, and Infrared Detectors for Astronomy VI, 915413, Montreal, Canada (2014).
[19] Nikzad *et al.* 2017, "High Efficiency UV/Optical/NIR Detectors for Large Aperture Telescopes and UV Explorer Missions: Development of and Field Observations with Delta-doped Arrays," *JATIS* 3(3), 03600

5 Minutes Integration Time Deep UV Pixel Development for "Ultrasat" Space Mission

Adi Birman[1], Omer Katz[1], Amos Fenigstein[1], Dmitry Veinger[1], Dmitri Ivanov[1], Shay Alfassi[1], Shirly Regev[2], Tuvia Liran[3], Ofer Lapid[3], Yossi Shvartzvald[3], Sagi Ben-Ami[3], Eli Waxman[3], Avishay Gal-Yam[3], Eran O. Ofek[3], Merlin F. Barschke[4], Rolf Bühler[4], Nirmal Kaipachery[4], Daniel Küsters[4], Julian Schliwinski[4]
[1]Tower Semiconductor, Shaul Amor 20, Migdal Ha'emek, Israel
[2]Etesian Semiconductor Ltd, P.O.B 3227, Ramat Yishai, 3004205, Israel
[3]Department of particle physics and astrophysics, Weizmann Institute of Science, Rehovot 76100, Israel
[4]Deutsches Elektronen-Synchrotron DESY, Platanenallee 6, 15738 Zeuthen, Germany

adibi@towersemi.com, Phone: +972-52-2401531

***Abstract*—This paper presents the pixel development for the Deep-UV sensor of "Ultrasat" space telescope. The 9.5um Pixel achieves 95dB dynamic range, QE of 80% at 240nm and Dark Current of 0.02 e/sec at -50C.**

Keywords—ultraviolet, Back Side illumination (BSI), Dark Current, Scientific Imaging

I. INTRODUCTION

The ULTRASAT Transient Astronomical Satellite [1,2], led by the Weizmann Institute of Science (WIS) and the Israel Space Agency (ISA), is planned to have a broad scientific impact across the fields of Gravitational Wave (GW) sources, supernovae, variable and flare stars, active galactic nuclei, tidal disruption events, compact objects, and galaxies. ULTRASAT is expected to be launched into GEO orbit in 2026 by NASA, carrying a UV space telescope with a large field of view, extremely sensitive in the wavelength range of 220 and 280 nm.

A custom 22.5-Mpixel UV BSI CMOS Image Sensor was developed to serve at the heart of this telescope. The camera is composed of 2x2 22.5-Mpixel sensors, utilizing a total sensing area of 90mm x 90mm.

To collect the weakest signal from the far end of the universe, the sensor integrates each frame for 5 minutes(!). Extremely low dark current is crucial for such long integration, which was achieved by careful pixel and array design, and by cooling the sensor to -70oC.

Pixel design's main challenges are: (1) a dynamic range larger than 92dB, (2) very high QE in the UV range, with an average larger than 60% in the 220-280nm range (3) extremely low dark current, less than 0.026 e/sec at -70°C.

A 9.5µm Dual-Gain Rolling-Shutter Pixel (Fig. 1) was designed and fabricated using the 180nm CIS BSI process of Tower Semiconductor. Pixel and process integration were optimized to meet these requirements.

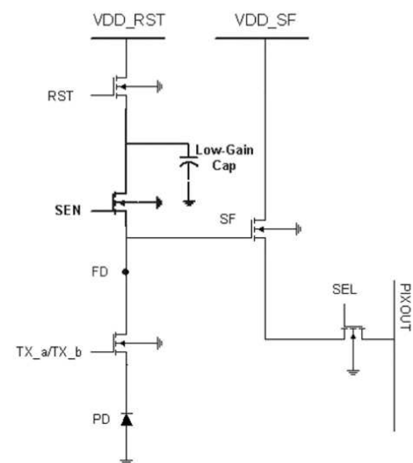

Fig. 1. The Pixel Schematics

II. PIXEL DESIGN – HIGH DYNAMIC RANGE

The high dynamic range of 95dB was established by the combination of (1) high conversion gain (100µV/e), (2) low noise source follower and (3) Full Well of 150Ke.

A special Transfer Gate and Floating Diffusion design [3] was used & optimized for a 2-Dimensional stitched process. A delicate adjustment of the layout was performed to enhance robustness to the allowed masks alignment variations, with no compromise on resulting device performance.

A dedicated Low-Noise Source Follower (SF) with a large enough gate area was chosen to find the optimal combination of tight noise distribution & low enough SF capacitance.

The Drain supplies of the pixel 'RST' & 'SF' transistors were separated to allow optimal operation under low light conditions (keeping the SF at Saturation mode for signal levels close to dark).

300 sec integration time puts a unique challenge to this application; maintaining very high Full Well at the Photodiode, while allowing very good low-light linearity, requires careful optimization of the pixel layout, operation & process.

Photodiode Pinning Voltage, Transfer Gate Isolation & Floating Diffusion doping affect some of the key pixel

parameters: Full Well, Signal Linearity, Anti-Blooming ability and sense-node capacitance.

These aspects were widely explored during the pixel development phase, and the optimal combination was applied on the 'Ultrasat' pixel.

III. Dedicated UV Anti-Reflecting Coating

In Backside illumination sensors there is more freedom to select ARC (anti reflecting coating) materials and thicknesses, compared to front-side illumination sensors, where the various layers which are a mandatory part of the front-end devices also affect the light absorption and reflection. The two main considerations for choosing a good ARC are: (1) High QE within the selected bandwidth, (2) Formation of an excellent surface passivation.

For Ultrasat mission, the goal was to optimize QE in the 220÷280nm band and try to minimize the QE for longer wavelengths.

The ARC must be solely composed of "Fab-Friendly" materials. In addition, it should not consist of too many layers/processing steps. Thus, we chose to use up to 6 layers for the ARC layers stack.

The 1st layer takes care of surface passivation. A well-known high-K material which is negatively charged, creates a thin accumulation layer of holes on the epi surface and eliminates dark current generation which could have been caused by surface states and dangling bonds.

Optical simulations were used to define the properties of the complete ARC layers stack and compare their expected performance.

Material types & layers thickness were carefully tuned to achieve maximal transmittance at the selected wavelength band and the typical incident angle of the telescope optical system. Several ARC options were chosen and implemented on a test sensor.

The chosen "UV-2" coating achieves Peak QE of 80% at 240nm and average of more than 60% for the 220-280nm band (Fig. 2,3).

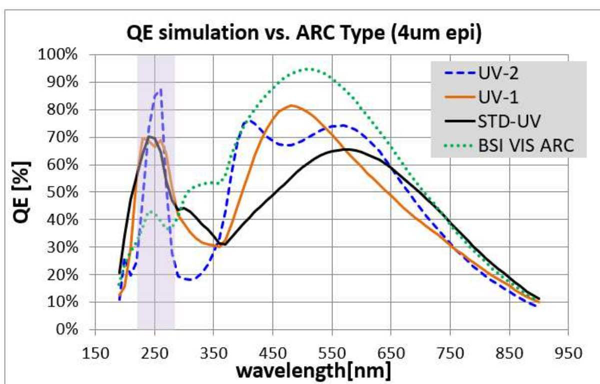

Fig. 2. Simulation of Quantum Efficiency vs. Anti-Reflective Coating Type. "STD" UV-ARC is compared with two options of UV-tailored ARC for the Ultrasat range of interest (220-280nm). The STD BSI ARC for visible light is also presented as a reference

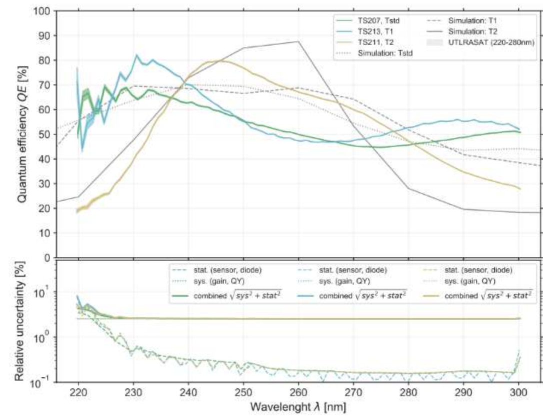

Fig. 3. Actual QE measurements of the 3 ARC flavours (UV-2 or "T2" was the chosen one)

IV. Dark Current Optimization & The "Optical Trench"

During the pixel and process development stage (conducted on a pixel design development sensor), we encountered an effect of light emission from on-chip peripheral circuitry (Fig. 4,5).

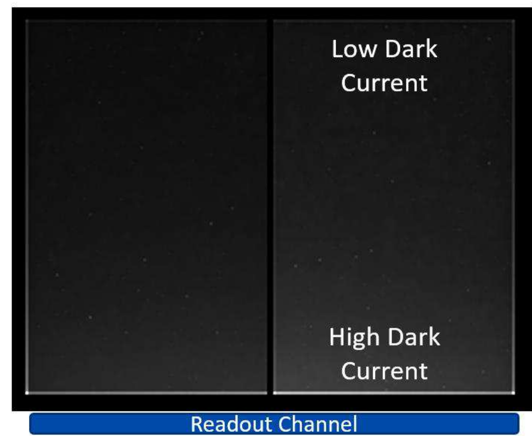

Fig. 4. Dark Image Affected by Nearby Circuits emission (Captured on the Development sensor, processed with no "Optical Trench")

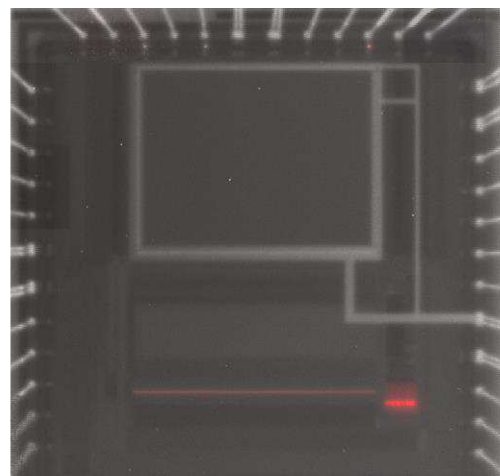

Fig. 5. Infrared Emission top image of the development sensor showing the glowing circuits. The Bright frame around the pixel array is the "Optical Trench"

This effect, historically known from scientific CCD sensors as "Amplifier Glow" [4], appears to be present and significant in high-end cooled BSI CIS as well, especially when observing faint light sources during long integration times[5].

Due to the high refractive index of the silicon versus the ARC/external media on one side and dielectrics of the CMOS backend on the other side, the emitted IR light is waveguided in the thinned epi-Si layer (Fig. 6).

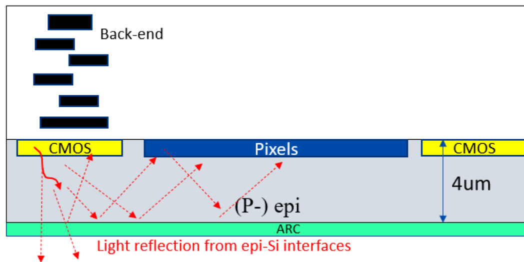

Fig. 6. NIR photons emission from the peripheral circuits

With no barrier to stop them, the emitted IR photons would slowly absorb along the pixel array epi layer, leaving a clear pattern of Dark Current gradient.

Different methods were used in the past to minimize this phenomenon (shut-off unnecessary circuitry blocks during exposure time, place other blocks as far as possible from the pixel array) but none of them could fully eliminate it.

Comprehensive analysis of this phenomenon led to a unique process development of a physical barrier that blocks circuit-emitted photons from reaching the pixel array. This physical barrier, named "Optical Trench" is a TSV-like structure, crossing the whole epi depth, coated with Aluminum to serve as a light block (Fig 7,8).

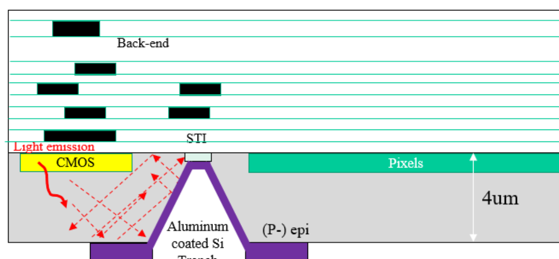

Fig. 7. Schematic drawing of the "Optical Trench", blocking the emitted NIR photons from reaching the pixel array

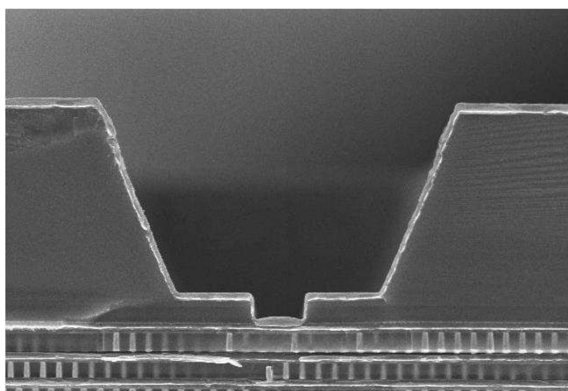

Fig. 8. SEM image of the "Optical Trench" (Pad area)

A sloped Silicon etch process (at the backside of the wafer) was developed to enable high quality metal coating inside the Optical Trench. The metal coating is connected to one of the chip's ground pads, and is separated from the EPI layer using an isolation layer.

Implementing the "Optical Trench" combined with several pixel and circuit design techniques helped solve this effect specifically (Fig 9,10) and achieve an overall Dark Current of 0.02 e/sec at -50ºC, which enables capturing a high-quality image at 300 seconds integration time.

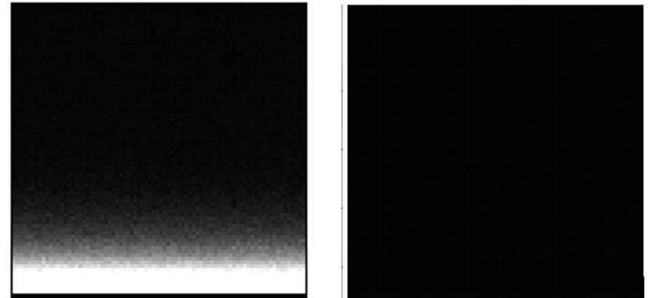

Fig. 9. Comparison of High-Gain Dark Images captured with "Ultrasat Sensor" (a small ROI at the bottom side of the Pixel Array is presented). On the left side – a sensor which was manufactured without the "Optical Trench". The 'glow' at the bottom rows is clearly seen. On the right side – the regular sensor, with "Optical Trench" – the 'glow' is fully eliminated

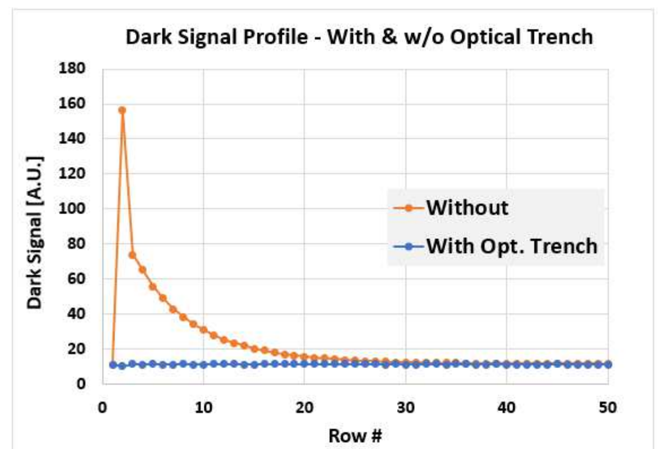

Fig. 10. Dark Signal Profile (of the 2 images shown on Fig.9)

V. Summary

In this paper we presented the main development challenges of the "Ultrasat" pixel and the ways we found to achieve all the design goals. The Pixel performance summary is described below (table 1).

The unique process and device features which were developed here didn't only contribute to the success of the Ultrasat mission, but also defined a path that enables a successful design of many other types of scientific CMOS Image Sensors.

TABLE I. PIXEL PERFORMANCE SUMMARY

Parameter	Ultrasat Sensor		
	Target	***Actual***	***Units***
QE (Avarage at 220-280nm)	>60	80 at 240nm AVG > 60	%
Conversion Gain (High Gain)	>90	>100	uV/e
Full Well Capacity (Low Gain) at 5 Minutes Integration	>140	>150	Ke-
Temporal Noise Floor	<3.5	<2.5*	e-
Dynamic Range	>92	95	dB
Dark Current at -70C	<0.026	0.02 at -50C*	e-/sec/pixel

*Wafer level test. Waiting for accurate data from packaged sensors

REFERENCES

[1] Bastian-Querner, Benjamin, et al. "Sensor characterization for the ULTRASAT space telescope." UV/Optical/IR Space Telescopes and Instruments: Innovative Technologies and Concepts X. Vol. 11819. SPIE, 2021.

[2] Liran, Tuvia, et al. "The design of a UV CMOS sensor for the ULTRASAT space telescope." Space Telescopes and Instrumentation 2022: Ultraviolet to Gamma Ray. Vol. 12181. SPIE, 2022.

[3] Fenigstein, Amos, Adi Birman, and Assaf Lahav. "Night Vision CMOS Image Sensors Pixel for Sub-mililux Light Conditions." Proc. Of. 2015.

[4] Tulloch, Simon M. "Photon counting and fast photometry with L3 CCDs." Ground-based Instrumentation for Astronomy. Vol. 5492. SPIE, 2004

[5] Wang, Xinyang, et al. "A 4M, 1.4 e-noise, 96dB dynamic range, back-side illuminated CMOS image sensor." Proceedings of the International Image Sensor Workshop. 2015..

Fabrication Of Small Pitch InGaAs Photodiodes Using In-Situ Doping And Shallow Mesa Architecture For SWIR Sensing

Jules Tillement[a,b,c], Cyril Cervera[b], Jacques Baylet[b], Christophe Jany[b], François Nardelli[b], Quentin Lalauze[b], Thomas Di Rito[b], Romain Paquet[b], Olivier Saxod[b], Norbert Moussy[b], Olivier Gravrand[b], Virginie Beugin[b], Sylvain Georges[a], Thierry Baron[c], François Roy[a], Frédéric Boeuf[a]

[a] STMicroelectronics, 850 rue Jean Monnet, Crolles, 38926, France – email: jules.tillement@st.com
[b] Minatec Campus, Leti, CEA, Grenoble, 38054, France
[c] Université Grenoble Alpes, CNRS, CEA/LETI Minatec, LTM, Grenoble, 38054, France

***Abstract*—This paper presents the complete design, fabrication, and characterization of a shallow mesa architecture for SWIR sensor. We characterized and demonstrated working photodiodes collecting 1.55 µm photons. The best measured dark current density for a 5 µm pixel pitch reaches 60 nA/cm² at -0.1V and at room temperature. 3 µm pixel pitch photodiodes are also demonstrated with higher dark current density and different strategies to lower it are discussed. The main contributors responsible for the dark current are investigated with perimetric contribution analysis and temperature measurements.**

Keywords*—*InGaAs, Mesa, SWIR, sensor, photodiode

I. Introduction

The development of short-wave infra-red (SWIR) sensors is led by the growing demand in various fields such as security, automotive, industry or agriculture. In the SWIR range between 1 and 2.5 µm, silicon is transparent ($\lambda_{cut,Si} = 1.1\ \mu m$) which leads to different material alternatives for the photon absorption. The main candidates are quantum films [1], $In_{0.53}Ga_{0.47}As$ [2]–[5] or Ge on Si [6].

$In_{0.53}Ga_{0.47}As$ (cut-off wavelength $\lambda_C = 1.7\ \mu m$) is latticed-matched to InP and has a lower band gap (0.74 eV at room temperature [7]) than Si suitable for SWIR collection. The state-of-the-art for InGaAs imager on Si read-out integrated circuit (ROIC) is a 5 µm pixel pitch with quantum efficiency (QE) greater than 75% at 1.2 µm. The dark current is reported to be as low as 2 nA/cm² at -0.1V and at 23°C [2]. The standard structure for an InGaAs-based SWIR sensor is a thick low doped n-InGaAs absorption layer epitaxied on an InP substrate. The small gap InGaAs layer is protected by an InP cap layer with a larger band gap (E_g = 1.34 eV at 25°C [8]). This way, InP is used as a first passivation layer to prevent the generation of dark current from InGaAs. Indeed, small band gap material such as InGaAs can easily generate dark current at room temperature. It is thus a priority to have the InGaAs absorption layer with the lowest possible defect density at interfaces and in the bulk. The crucial process step is the definition of each pixel by the creation of a p/n junction. Literature reports different alternatives for this purpose such as Zn diffusion [2], [3], [9], Be implantation [10], [11] or shallow mesa-type architecture [12], [13].

Today, the standard process to create the p/n junction is done by Zn diffusion. First, the dielectric is opened on top of the epitaxial stack, then Zn is diffused from this hole and reaches the InGaAs absorption layer to create the p^+-type region. The left-hand side of Fig. 1 shows the schematic cross section of the photodiode after the diffusion process. The isotropic behavior of the diffusion is a clear issue as the target of this work is to reduce the pixel pitch. In addition to this isotropic diffusion, it has been shown that Zn diffuses faster at the InP/InGaAs interface [14] i.e. laterally. Therefore, the diffusion process might be an issue to reduce the pitch because of its acceleration in the lateral direction which might result in a unique p-type region for all the neighboring pixels.

Be implantation could be an interesting solution to overcome the issue of lateral diffusion. Implantation is commonly used in the Si processes to precisely locate the dopants in the structure. The main drawback of the implantation is the introduction of many defects in the structure. It is mandatory to cure as many defects as possible during the anneal to avoid the generation of dark current. Curing defects in InP/InGaAs is not easy and the published dark current is at best in the range of µA/cm². This is a path we study but out of the scope of this paper [11].

The shallow mesa-type architecture could be a solution to reduce the pixel pitch and to target state of the art performance in terms of dark current and QE. Only a few groups report the study of shallow mesa architecture [12], [13], [15]. In this manufacturing method, the structure is doped in-situ during the epitaxy of the stack and the p/n junction definition is done by etching the top p-type layer between the pixels. Unlike other processes for mesa-type device fabrication, our etching step only removes the p-doped region from the top stack. The final schematic structure is presented on the right-hand side of Fig. 1 and referred as shallow mesa architecture. The pixel pitch is thus limited by the lithography and etching tools used in the process. The stack must be carefully designed to allow the collection of photo-carriers generated in the InGaAs absorption layer (color: light blue in Fig. 1). In addition, this alternative is a low thermal budget process which is an asset for the full integration on Si ROIC.

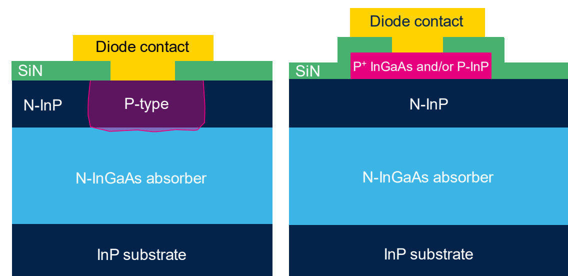

Fig. 1. Schematic cross section of the photodiode after different processes. On the left-hand side, the photodiode after the Zn diffusion or Be implantation processes. On the right-hand side, the photodiode after the shallow mesa-type process

XXX-X-XXXX-XXXX-X/XX/$XX.00 ©20XX IEEE

II. Design

The goal of the designed structure is to collect the photo-carriers from the InGaAs absorption layer through the heterojunction created by the n-InGaAs on n-InP. This n-InP cap passivates the small gap layer as explained before, but the heterojunction introduces an unfavorable barrier to the hole collection as it is represented on the band diagram Fig. 2. The challenge is to tune three key parameters to design a structure that collects photogenerated holes at the p-type contact layer (left side of the band diagram on Fig. 2). These parameters are the doping and thickness of the barrier n-InP layer and the doping concentration of the contact layer. It allows to monitor the electric field applied to the device to collect the carriers through the heterojunction.

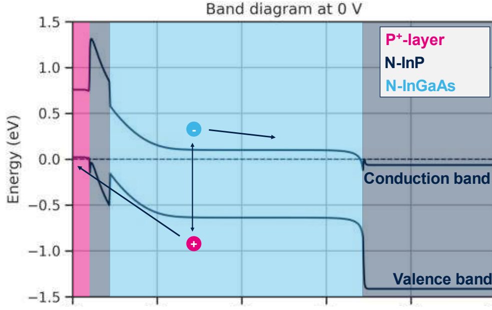

Fig. 2. Band diagram of simulated structure at equilibrium with the photogenerated pair schematicaly represented and their path of collection

The targeted structure should collect the carrier from InGaAs at low reverse bias. The dark blue curve on Fig. 3 shows a well-designed structure where the current from InGaAs is collected at quasi null voltage. If the n-InP barrier layer is too thick (left-hand side in pink) or too doped (right-hand side in pink), it increases the electrostatic barrier and blocks the carrier at low bias. On the other hand, if the n-InP cap is too thin to minimize the electrostatic barrier, it infers process constraints during the p-layer etching process that is difficult to control uniformly on the wafer.

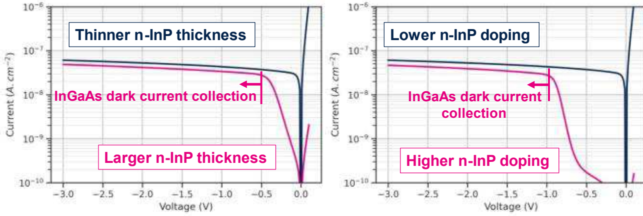

Fig. 3. Effect of barrier thickness and doping on the simulated dark current

Intrinsic material parameters are based on the literature [16], [17] and quality related parameters are fitted on photodiode measurements. This theoretical study allowed us to find a set of doping concentrations and thicknesses parameters that suppresses the barrier for hole collection.

III. Fabrication

The schematic and simplified process of the shallow mesa-type photodiode is represented on Fig. 4. All layers with their final doping and thickness are epitaxied on a 3'' InP substrate. Then, pixel definition is performed by etching the p-type layer. After that, the device is passivated with a dielectric. The final step is the fabrication of both contacts.

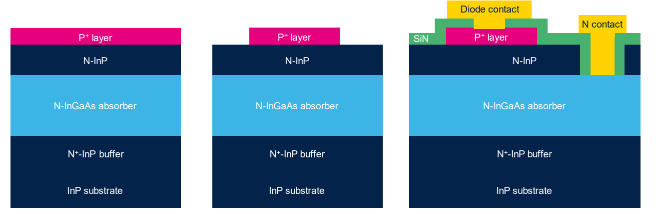

Fig. 4. Simplified schematic process flow of the shallow mesa-type process

This paper investigates the crucial process step of passivation with a first structure using a p-InP layer as the contact layer (referred as processes A1 and A2). Each process has a different nitride deposited with a different gas flow ratio. These dielectrics will have a great impact on the dark current. Then, we will analyze a second structure using a dual layer of p^+-InGaAs on p-InP as the contact layer (referred as process B). The additional p-InGaAs layer in process B allows a better diode contact than p-InP layer. Fig. 5 is a SEM view of the top of the structure. It is clearly visible that the pixels are defined by etching the p contact layer.

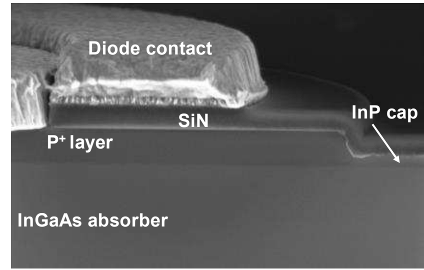

Fig. 5. SEM view after the whole process

IV. Characterization

A. *Impact of passivation on dark current*

Two different processes are compared here to define the best dielectric for the realization of small pitch photodiode with the lowest dark current possible. If we focus on the dark current measurement presented Fig. 6, we see a different evolution with reverse bias directly related to the different passivation. This difference could indicate different dark current sources. At -0.5V and at room temperature, the dark current for process A1 reaches $5 \cdot 10^{-13}$ A and for process A2, it reaches $2.8 \cdot 10^{-13}$ A.

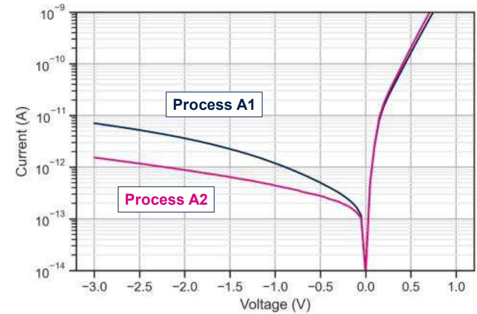

Fig. 6. Dark current measurement on 15 µm pitch in-array photodiodes. The curve is the median of more than 100 diodes measured

Diodes of different sizes ranging from 10 µm to 120 µm were measured to characterize contributions from the bulk (J_b) and from the periphery (J_p) based on the following equation.

$$I_{total} = A * J_b + P * J_P \quad (1)$$

A is the area of the diode defined by its p-layer diameter and P is the perimeter of the diode defined by the perimeter of the p-layer (see cut in Fig. 4). Measured photodiodes have different P/A ratio leading to plot I/A = f(P/A) and discriminate J_b and J_p with a simple linear regression. In our case, Fig. 7 shows the very different value of J_p for the two cases. As our goal is to reduce the pixel pitch, the contribution from the perimeter over the one from bulk is more and more important. Here, the bulk contribution is even for the two processes as $J_b = 2 \cdot 10^{-11} A/cm^2$ in both cases. For the perimetric one, in process A1, $J_P = 8 \cdot 10^{-11} A/cm$ and for process A2, $J_P = 4 \cdot 10^{-13} A/cm$. The perimetric contribution is drastically reduced in process A2 which infers that process A2 is much more suitable for small pixel pitch fabrication.

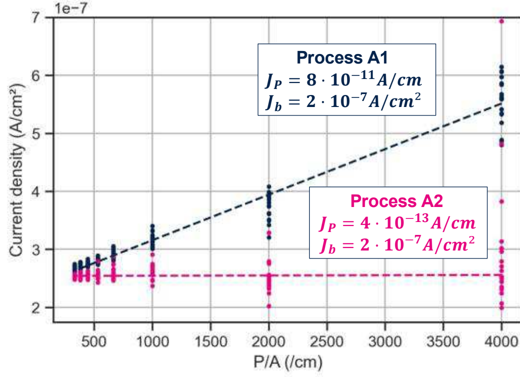

Fig. 7. Perimetric and bulk contribution to the global dark current from measurements performed on diodes with diameter ranging from 10 to 120 µm

Capacitance measurements were also carried out on metal – insulator – semiconductor (MIS) structures to compare the two dielectrics. What is visible on Fig. 8 is the difference between the two hysteresis after the same ramp of polarization. The hysteresis is directly proportional to the charge trapped in the dielectric [18]. Relatively, the passivation of process A2 traps less charges than process A1. As these charges could alter the device's performance, it is thus very important to minimize the effect of trapping in the final device.

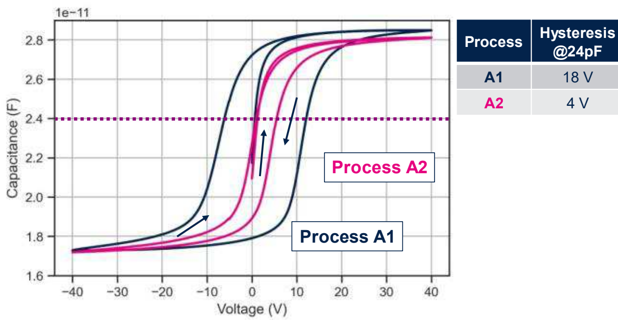

Process	Hysteresis @24pF
A1	18 V
A2	4 V

Fig. 8. Capacitance measurement on metal – insulator – semiconductor structure. The MIS structure is a 300µm diameter circle. The measurement starts at 0V then ramp to +40V then goes to -40V and ends at +40V. The hysteresis in V given in the table is computed as the absolute difference between extrema at $2.4 \cdot 10^{-11}$ F.

The deposited nitride in process A2 will now be integrated on the second structure i.e., process B. Performances of this process are investigated in the following part.

B. Characterization of SWIR photodiodes

The collection of SWIR photons can be verified at wafer level. In the measurement set-up, a 1.55 µm led is embedded inside the prober and it is possible to switch it on or off. The result of the measurements on bundles of one hundred 3 µm pixel pitch photodiodes are presented Fig. 9 and show the collection of the photons at 0V. This indicates that there is no electrostatic barrier for the carriers generated in the InGaAs layer. These tests demonstrate the fabrication of working InGaAs SWIR photodiodes with such small pitch.

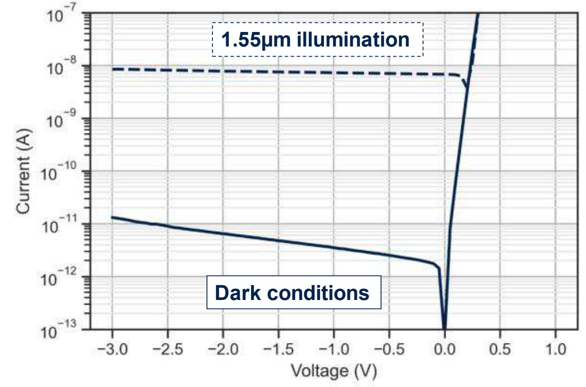

Fig. 9. Median current measurement for bundles of one hundred 3 µm pixel pitch photodiode under dark and SWIR illumination. The solid lines represent the dark current and the dotted lines current under 1.55 µm illumination

The current is measured on bundles of multiple diodes because the dark current from a single diode is too low. Here we measure 1.75pA at -0.1V and at room temperature.

C. Dark current analysis

Dark current is a very important figure of merit for photodiodes. Improving it allows to increase the signal over noise ratio which leads to a detection of better quality.

Fig. 9 presents the dark current at room temperature (solid line) for a 3µm pixel pitch. For a deeper understanding of the dark current generating phenomena occurring in the different devices, we performed temperature measurements. The hypothesis done here is that all current coming from InP are negligible as its band gap is around twice the one from InGaAs. When the dark current is limited by Shockley-Read-Hall (SRH) generation-recombination (GR), the current is proportional to $T^{3/2} \exp(E_{g,InGaAs}/2kT)$. If the dark current is limited by the diffusion, the current is proportional to $T^3 \exp(E_{g,InGaAs}/kT)$. Dotted lines in Fig. 10 are the evolution of the current with temperature if it is purely limited by diffusion (light blue) or by GR (pink) in the InGaAs absorption layer. These tests were done on bundle of a hundred 5 µm pitch diodes and the results are presented Fig. 10. The evolution of the current with the temperature is presented for two different reverse biases.

For both polarizations and high temperatures, the dark current must be limited by the diffusion in the InGaAs absorption layer whereas for lower temperatures, the limiting dark current phenomenon seems to depend on the polarization. For high reverse bias of -1.5V, the evolution

of the dark current follows the pink dotted line which indicates a GR limitation whereas for low reverse bias, it is a mix of both diffusion and GR.

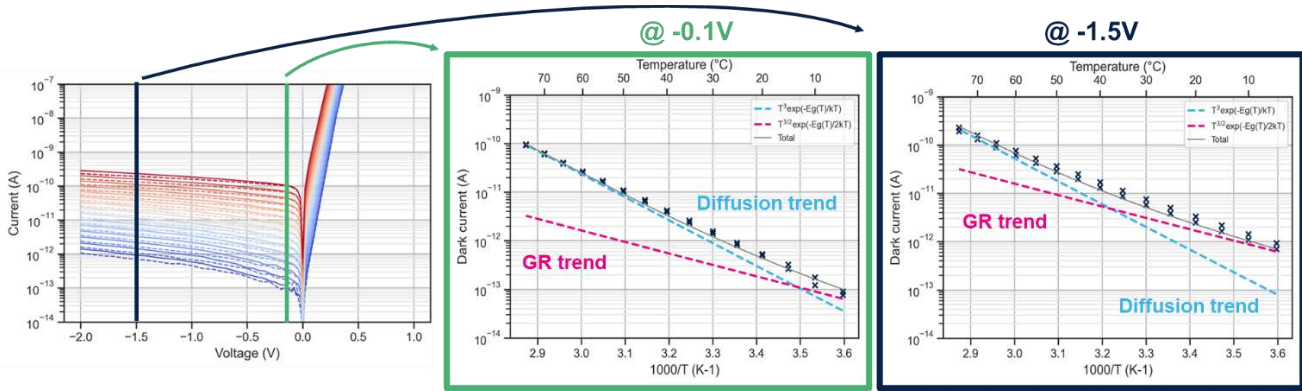

Fig. 10. Temperature measurement on a bundle of one hundred 5 µm pixel pitch diodes. On the right-hand side, we compare the evolution of the measured dark current with the theoretical evolution of the current lilmited by diffusion (light blue dotted line) or generation recombination (pink dotted line) for two polarizations: -0.1V and -1.5V.

As an overall comparison, we gathered the best results measured and compared it to all the different alternatives for the fabrication of InGaAs photodiodes on Fig. 11. Zn diffused diodes in pink is the standard process for InGaAs photodiode fabrication and reaches 2 nA/cm² for the best case at 5 µm pixel pitch [2]. In pink, Be implantation process shows the highest dark current for the fabrication of the photodiodes [11]. Our shallow mesa photodiodes have a lower dark current than the InGaAs mesa/shallow mesa state-of-the-art but around one decade higher than the state-of-the-art for 5 µm pixel pitch. From 15 to 5 µm pixel pitch, our diodes show a flat dark current density of about 60 nA/cm². The measurement for 3 µm pixel pitch is the first published for a pitch that small with a dark current density of 200 nA/cm². This increasing dark current density when the pitch reduces is still under investigation. The impact of charges in the dielectric or traps at the dielectric/cap interface could have great impact on the dark current and is a clear way to improve the dark current density of the small pitch photodiodes.

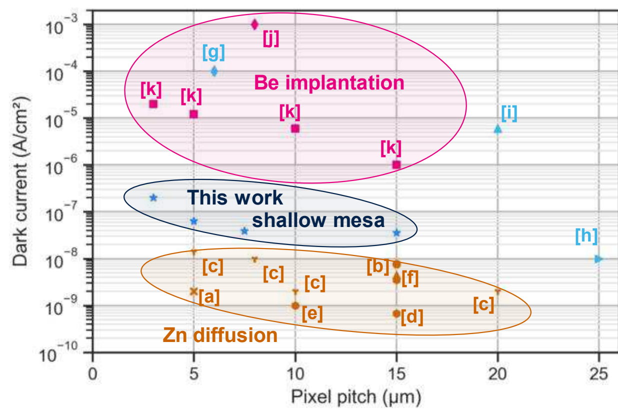

Fig. 11. Comparison of the different alternatives for the fabrication of InGaAs photodiodes. References on the graph give the condition of the measurement if found and the article it comes from: [a] 23°C @-0.1V article: [2] - [b] 30°C @-0.2V article: [3] - [c] 22°C @-0.1V article: [5] - [d] 20°C article: [4] - [e] 20°C article: [19] - [f] RT @-0.3V article: [9] - [g] RT @-1V article: [12] - [h] 22°C @-0.1V article: [15] - [i] RT @-1V article: [20] - [j] @-1V article: [10] - [k] RT @-1V article: [11]

V. Conclusion

We demonstrated InGaAs photodiodes with this very promising innovative shallow mesa-type architecture. We reached dark current as low as 60 nA/cm² at -0.1V at room temperature for 5 µm pixel pitch. For lower pitch down to 3 µm, the dark current density increases to 200 nA/cm² but many improving path have been identified. Further investigations with simulations and capacitive measurements will continue to quantify the impact of the charge in the dielectric and the interface with the top layer. This promising architecture is now under study to be part in a complete integration in a CMOS fab.

References

[1] J. S. Steckel, A. G. Pattantyus-Abraham, E. Josse, E. Mazaleyrat, and K. Rochereau, *Dig. Tech. Pap. - SID Int. Symp.*, 2021

[2] S. Manda *et al.*, *Tech. Dig. - Int. Electron Devices Meet. IEDM*, 2019

[3] A. Rouvié *et al.*, *Infrared Technol. Appl. XLI, SPIE*, 2015

[4] R. Fraenkel *et al.*, *Infrared Technol. Appl. XLIII*, 2017

[5] H. Yuan, M. Meixell, J. Zhang, P. Bey, J. Kimchi, and L. C. Kilmer, *Infrared Technol. Appl. XXXVIII*, 2012

[6] A. Aliane, W. Ludurczak, L. André, and H. Kaya, *Semiconductor Science and Technology* 2020.

[7] S. Paul, J. B. Roy, and P. K. Basu, *J. Appl. Phys.,* 1991

[8] Z. Hang, H. Shen, and F. Pollak, *Solid State Commun,* 1990

[9] M. H. Dolas, O. Atesal, M. D. Caliskan, A. Bek, and E. Ozbay, *Infrared Sensors, Devices, Appl. IX*, 2019

[10] C. L. Chen *et al.*, *IEEE Int. Conf. 3D Syst. Integr. 3DIC, 2009*

[11] J. Tillement *et al.*, *Solid State Devices and Materials*, 2022.

[12] C. L. Chen *et al.*, *Microelectron. Eng.*, 2011

[13] M. H. Dolas, K. Circir, and S. Kocaman, *Image Sens. Technol. Mater. Devices, Syst. Appl. IV*, 2017

[14] A. Djedidi, A. Rouvie, J. Reverchon, M. Pires, N. Chevalier, and D. Mariolle, *Conf. Proc. - Int. Conf. Indium Phosphide Relat. Mater.*, 2012

[15] J. F. Klem, J. K. Kim, M. J. Cich, G. A. Keeler, S. D. Hawkins, and T. R. Fortune, *Appl. Phys. Lett.*, 2009

[16] R. K. Ahrenkiel, R. Ellingson, S. Johnston, and M. Wanlass, *Appl. Phys. Lett.*, 1998

[17] D. Vignaud, J. F. Lampin, E. Lefebvre, M. Zaknoune, and F. Mollot, *Appl. Phys. Lett.*, 2002

[18] D. Schroder, Semiconductor material and device characterization, 2006

[19] R. Fraenkel *et al.*, *Infrared Technology and Applications XLII*, 2016

[20] K. Circir, M. H. Dolas, and S. Kocaman, *Infrared Phys. Technol.* 2019

Evaluating the Theoretical Optical Performances of Colloidal Quantum Dot Thin Films for Infrared Imaging

Arthur Arnaud[1], Bilal Chehaibou[1,2,3], Gabriel Mugny[4], L Baudoin[1], P Machut[3,4], B Rae[5], A G Pattantyus-Abraham[6], Jonathan Steckel[4], Peter Reiss[3], Christophe Delerue[2]

[1] *STMicroelectronics, Digital FMT, Technology for Optical Sensors, Crolles, France*
[2] *Univ. Lille, CNRS, Centrale Lille, Univ. Polytechnique Hauts-de-France, Junia, UMR 8520 - IEMN, F-59000 Lille, France*
[3] *Univ. Grenoble Alpes, CEA, CNRS, IRIG-SyMMES, STEP, 38000 Grenoble, France*
[4] *STMicroelectronics, Analog, MEMS & Sensors Group, Imaging, Grenoble*
[5] *STMicroelectronics Analog, MEMS & Sensors Group, Imaging, Edimburgh, Scotland, UK*
[6] STMicroelectronics, Digital FMT, Technology for Optical Sensors, Fremont/Santa Clara, CA, USA

Abstract— **Research on the development of thin films made of colloidal Quantum Dots (CQDs) has progressively gained interest due to their optoelectronic properties and potential low-cost manufacturing. The ability to tune the first absorption feature of CQDs by changing their material composition, particle size and shape, and/or the surrounding dielectric environment (ligands) is particularly interesting for improving the performance of image sensors in the Near-Infrared (NIR) and Short-Wave Infrared domain (SWIR) where silicon poorly absorbs photons or has no absorption at all. To date, few papers have attempted to evaluate the best optical performances that can be achieved with CQD thin films. In this work, we present the results from our compact model mixing tight-binding simulations, effective medium theory and optical simulations, to explain the various factors impacting CQD photodiode performance and to compare their performance with classical bulk semiconductors like silicon, germanium and III-V's.**

Keywords—Colloidal quantum dots, Image sensors, SWIR, NIR, tight-binding, effective medium theory

I. Introduction

Since pioneering works by Ekimov, Efros and Brus in the 1980s [1], research on colloidal quantum dots (CQDs) has rapidly progressed, moving from academic research to the display industry and now to the microelectronics industry. Their excellent optical properties due to their exciton quantum confinement capability, as well as the low production costs related to their chemical synthesis and the easy large-scale integration into standard microelectronic flows have already allowed the development and commercialization of TV displays, and lighting solutions. Their ability to operate in ranges covering the ultraviolet, visible, and infrared, leveraging electrically passive optical-optical transduction, where the absorption of photons by CQDs are re-emitted at precisely engineered wavelengths determined by the size of the nanocrystals and the material from which they are made is very unique [2].

The use of CQDs for image sensors or photovoltaic cells is more complex because it requires the development of thin layers of nanocrystals with high optical absorption coefficients and good electronic properties to allow the transport of photogenerated charges towards the collecting electrodes [3,4]. The use of photodiodes based on CQDs is unlikely to compete with the use of silicon as a photodetector in the visible range, but it is very promising in the regions of the optical spectrum where silicon is less sensitive, especially in the NIR and SWIR portion of the spectrum where silicon becomes almost transparent. For these parts of the light spectrum, the most used bulk semiconductors are III-V materials such as InGaAs which can provide quantum efficiencies close to 100% with epitaxies of about 2 micrometers thickness. However, the use of an InGaAs photodiode to make image sensors is both complicated and expensive, due to the use of InP wafers for the realization of InGaAs epitaxy, but also due to the need for die-to-die or die-to-wafer hybridization to make functional image sensors. The resulting prohibitive costs (>1000$ per unit) currently limit their deployment for consumer applications. For infrared imaging applications, the use of CQDs is particularly attractive to reduce the cost of the sensors to a few dollars per unit thanks to their easy integration. At the same time, QD technology is also particularly suitable for applications requiring active light systems like Direct and Indirect Time-of-Flight (ITOF, DTOF) and structured light applications, where the presence of sharp excitonic peak due to the first $1s_e$-$1s_h$ transition allows improving the rejection rate of the solar background at the solar spectrum local minima, around the 940 nm, 1130 nm, and 1360 nm wavelengths.

To improve the performance of image sensors using CQD thin films as absorbers, it is necessary to understand and model accurately their optical properties and to understand the role of the nanoparticles and the ligands used to passivate the interface states on the surface of the nanoparticles. In this paper, after a brief presentation of the architecture of CQDs image sensors, we will present a complete physical model using Empirical Tight-Binding Method (ETBM) to evaluate the intrinsic optical properties of the nanoparticles, the Effective Medium Theory to calculate the optical indices of the thin films, and the transfer matrix method to optimize the performance of the photodiodes integrating these same thin films within a resonant cavity. Thus, we will be able to compare the maximum theoretical optical performances of CQDs made of different semiconductor materials with other bulk semiconductors such as InGaAs, germanium, silicon and silicon-germanium, and to show the interest in using quantum confinement to boost the sensitivity of image sensors for infrared sensing applications.

II. Colloidal quantum dots diode model

A. Generic structures of CQDs photodiodes

Although the CQD-based image sensors presented in the literature [5-8] can diverge in terms of design options for the photodiode signal readout, or on the choice of the CQD materials (PbS, HgTe, InAs...), most of them are based on the integration of a vertical CQD photodiode built above the Back-end-of-Line (BEOL), with the collection of the photogenerated charges on the photodiode bottom electrode (Fig.1). The integration of the active layer of passivated QDs is generally performed by full-wafer spin-coating of the colloidal QDs, with a replacement of the long-chain ligands by short-chain ones, realized either before deposition in solution (solution ligand exchange) [9], or directly on the wafer (solid-phase ligand exchange, which may require a layer-by-layer process) [10]. The realization of a photosensitive layer continuous over the full pixel matrix and above the metal interconnections has two advantages beyond its simple realization: it allows to obtain pixels with a 100% fill factor, but also the reduction of the pixel pitch, as the photodiode is no longer integrated at the silicon surface as the transistors of the pixel. With this approach, we have demonstrated the operation of a global shutter pixel with a pitch of 1.62um with 50% of EQE at 940 nm and 60% of EQE at 1400 nm [5].

Even if ligands are not directly involved in the film's light absorption (though they modulate the properties of the film as we will

XXX-X-XXXX-XXXX-X/XX/$XX.00 ©20XX IEEE

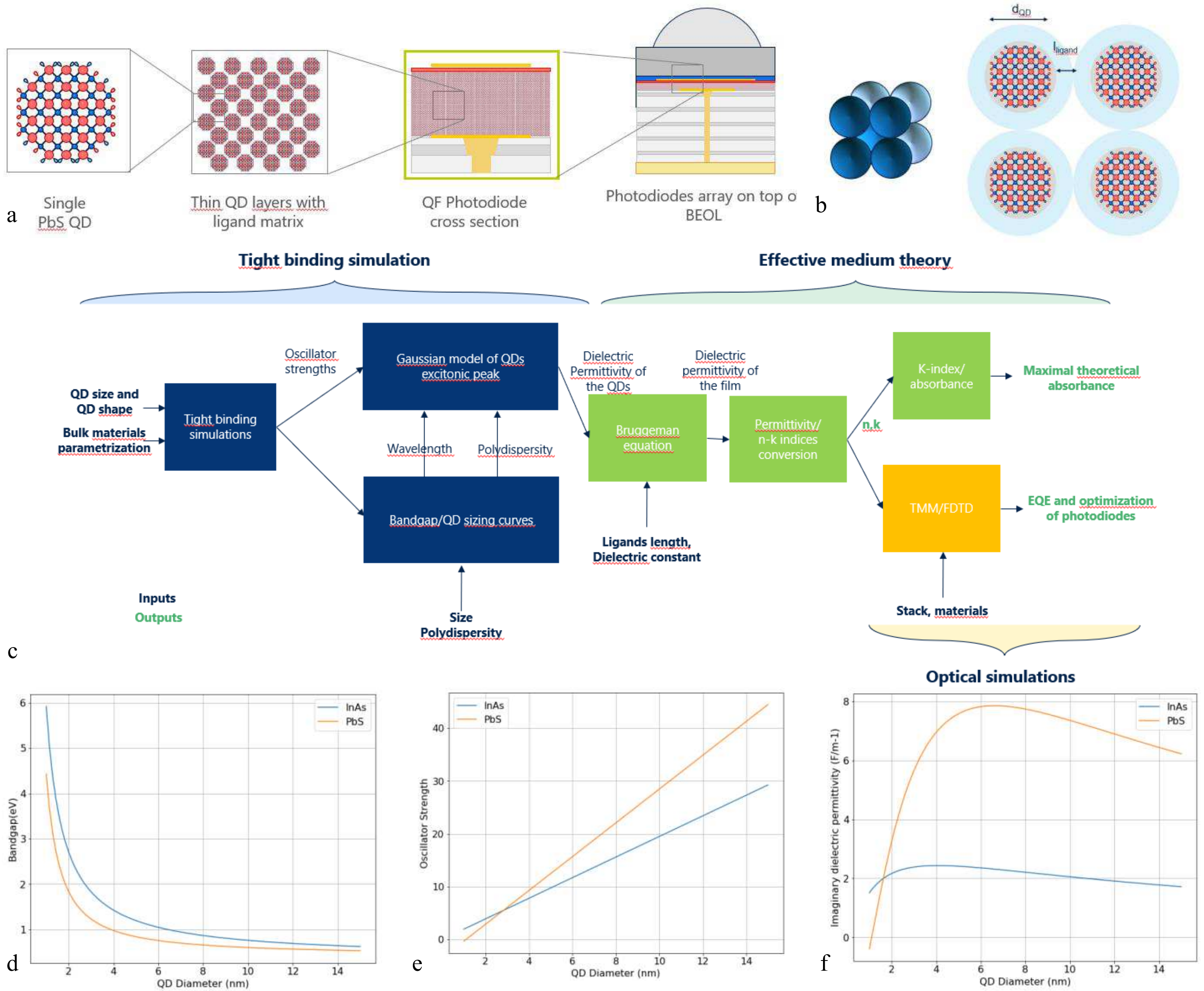

Figure 1. a. Generic scheme of the integration of a CQD photodiode above BEOL. b. Simplified scheme of close-packed passivated QDs inside thin films. c. Diagram representing the compact model stages. d. Polynomial fit of the optical bandgap of QDs vs QD diameter for PbS and InAs. e. Linear fit of the oscillator strength for PbS and InAs QDs. f. Extraction of the imaginary dielectric parts for PbS and InAs QDs.

show here), their choice is important for the operation of the photodiode. Passivation of the interface states by the ligands primarily reduces trapping and recombination phenomena in the film, improving the dark current of the photodiode. The use of short-chain ligands to passivate CQDs is also required to increase the density of QDs in the film but also to improve the electrical transport properties of the film, as the photogenerated charges pass from one QD to the other through a mechanism of variable-range hopping [11]. The ligands having a non-zero net charge, they also participate in the effective film doping [12] and also modify the workfunction of the QD layer through their dipole moment creating a local electric field around the QDs [13]. This last property enables the creation of heterojunctions by using different types of ligands within the same photodiode. Finally, they contribute to the mechanical and chemical stability of the thin films.

In this paper, we will only focus on the optical properties of CQD thin films. To understand the impact of the QDs and ligands properties on the photodiode performances, we developed a multiscale compact model represented in Fig.1c, based on the combined use of ETBM [14] to simulate the dielectric properties of isolated QDs, of the Bruggeman equation to describe the properties of CQD thin films, and finally of the Transfer Matrix Method to compute the performance of vertical photodiode stacks. The QDs' physical parameters taken into account are their size and shape, the properties of the semiconductor they are made of, and the size polydispersity, a parameter controlled during their chemical synthesis. In the case of ligands, we only consider their effective length and their optical indices.

B. *Intrinsic properties of QDs*

First, the electronic structure of the nanocrystals was calculated using the TB_Sim software [14] to describe the evolution of the optical bandgap and the oscillator forces of the QDs as a function of the size of the QDs, their geometry and the semiconductor material from which they are made. The interest of ETBM over Density Functional Theory (DFT) method is to quickly calculate the oscillator strengths for QDs of several nanometers without being limited by the computational resources. The compilation of these two data, oscillator forces and optical bandgap, allows us to extract the coefficients specific to the QD materials, to approximate optical bandgap variations with $1/d_{QD}$ polynomials (Fig.1d) and oscillator strength with linear regression as explained in [14] (Fig.1e). Finally, we use the two latter quantities along with the size polydispersity to input an analytical equation of the imaginary part of the dielectric permittivity Im[ε] [14]. It allows us to evaluate Im[ε] at the first exitonic peak for a broad range of QD sizes as shown in Fig 1.f for lead sulfide and indium arsenide QDs.

III. PERFORMANCE OF CQD THIN FILMS

A. CQD thin film dielectric model

Once the properties of the isolated QDs have been modeled, it is necessary to understand the dielectric interactions between the QDs and the ligands and how they affect the optical properties of the thin films. To do so, we must first make simplifying assumptions on the arrangement of the QDs within the thin films by considering that the QDs passivated by the ligands tend to be organized in a body-centered cubic superlattice within the thin films [15]. The fact that ligands are short, and the results presented in [17] allow us to assume that each passivated QD behaves as a rigid sphere. It is then possible to define the packing of the nanocrystals superlattice and to calculate the QDs' density within the film as a function of the QD diameter and the ligand length. This calculation is mandatory for the implementation of Bruggeman's effective medium approximation which accurately describes the dielectric behavior of CQDs thin films [16,17], by using the n and k indices of the QDs. These are derived from the QDs' dielectric constant imaginary part, the bulk semiconductor dielectric constant real part and the refraction index of the ligands as extracted in [17] (ligands do not contribute to the absorption (k_{ligand}=0)).

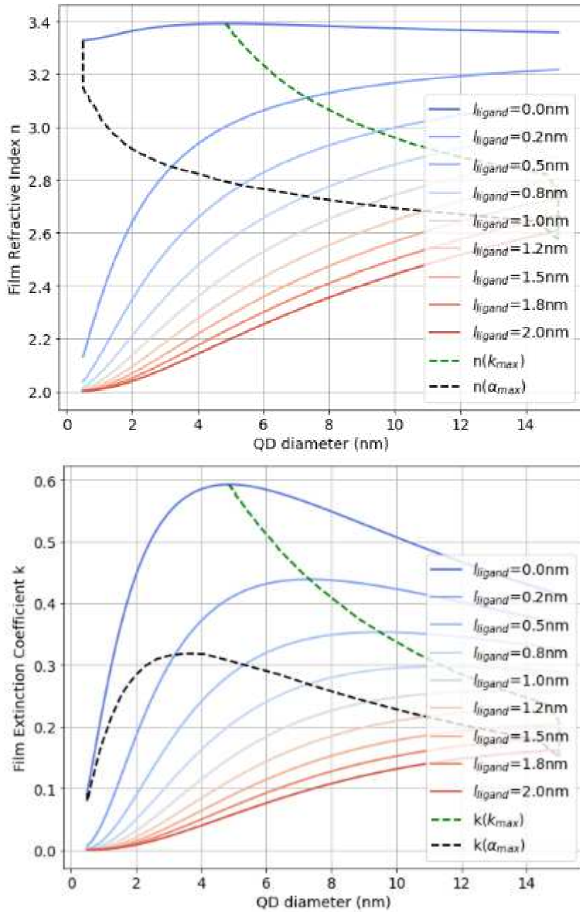

Figure 2. Evolution of the refractive index (a) and extinction coefficient k (b) of PbS QDs with 4% size polydispersity for several ligand length values.

B. Influence of ligand length

Figure 2 illustrates the dependence of n and k indices of thin films on QD's diameter for various ligands length assuming a size polydispersity of 4%. These curves first demonstrate the interest in reducing the inter-QD distance to densify CQDs thin films to finally increase the probability for a QD to capture a photon. The second interesting observation is the existence of an optimal QD size for each fixed ligand length that maximizes the extinction coefficient k or the absorption coefficient (not represented here) whose loci are represented by a dashed curve in Fig.2. The existence of this optimum can be explained by the fact that whereas decreasing the QD size helps to enhance the quantum confinement and extinction coefficient of individual QDs first, below a given diameter, the reduction of QDs' size strongly impacts the QDs volume fraction in the film, counterbalancing the confinement effect, hence leading to a reduction of the absorption coefficient of the thin film.

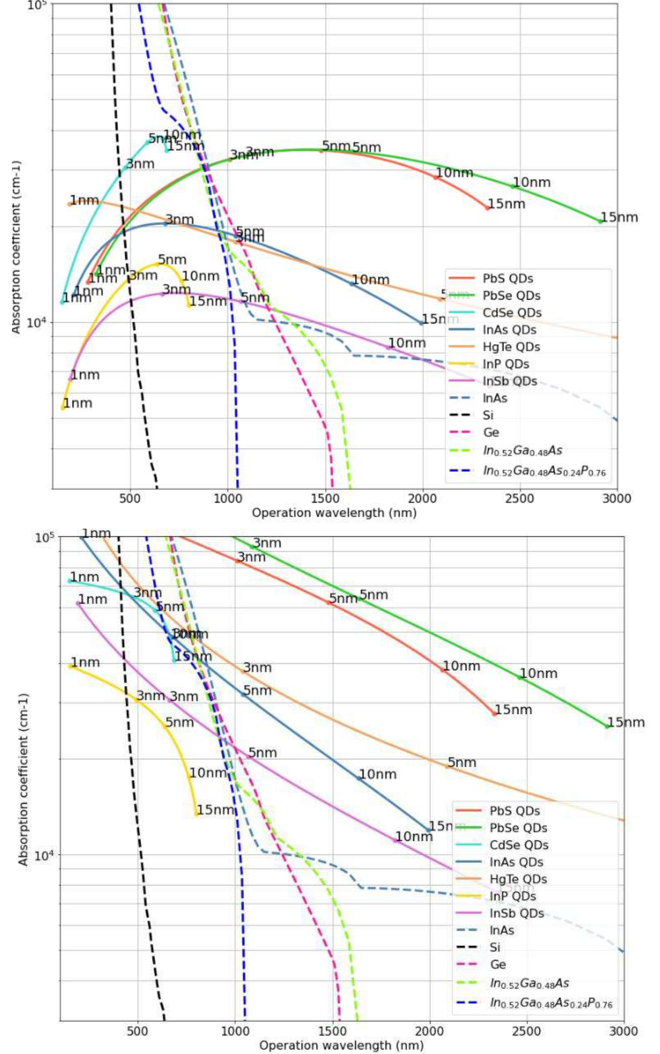

Figure 3. a. Evolution of the absorption coefficient of QDs at the excitonic peak wavelength for a ligand length of 0.4 nm and a size dispersity of 4%. b. Optical performances assuming the formation of superlattices of connected quantum dots.

C. Comparing quantum dots materials with other semiconductors

The previous study performed on lead sulfide QDs has been systematically performed on other semiconductor materials: PbSe, CdSe, InP, InAs, InSb, and HgTe. Fig. 3 compiles the absorption coefficients for all these materials as a function of the wavelength of the first excitonic peak to compare CQDs materials with each other and with other bulk semiconductors, without any reference to QDs' diameters but only to the application wavelength. Fig.3a shows the performances of QDs passivated with 0.4 nm-long ligands and 4% polydispersity while Fig.3b shows the performances of thin films with QDs touching each other [18]. These two graphs demonstrate that it is easily possible to exceed the optical performances of silicon with InAs, InSb, HgTe, PbS and PbSe CQDs in the infrared but also to create highly absorbent thin films performing better than Germanium and III-V for wavelengths above 1.0 µm by improving QDs size polydispersity and inter-QDs distance.

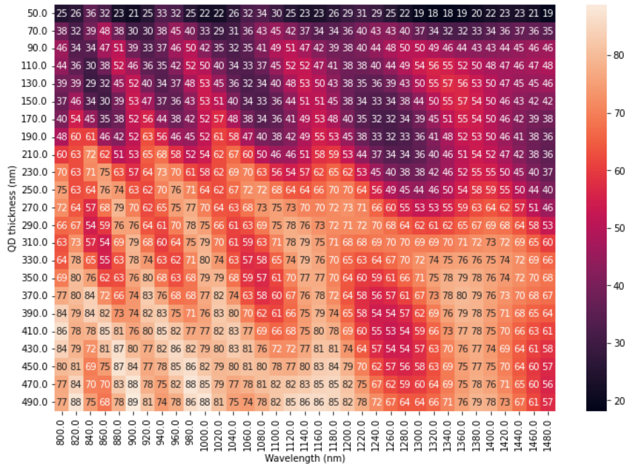

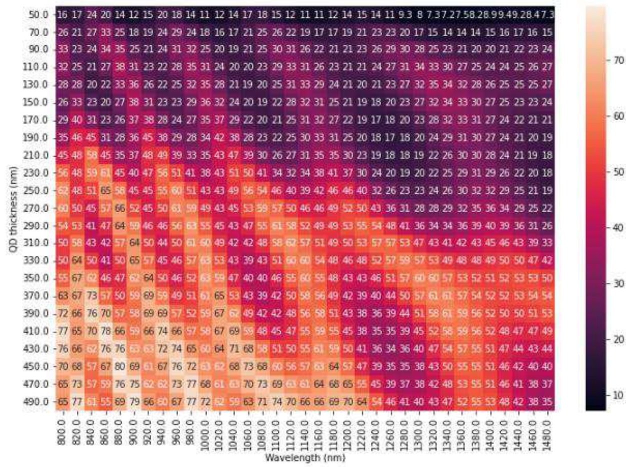

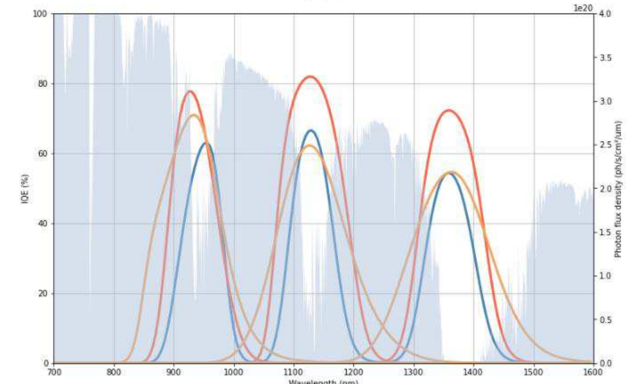

Figure 4. a. EQE maps assuming 4% size dispersion and 0.4 nm-long ligands for PbS (a) and InAs (b). c. Performances of photodiodes at the excitonic peak wavelength, with a QD layer thickness around 300 nm for the same size dispersion and ligand length (red: PbS, orange: InAs, Blue: HgTe). Absorption of QDs at higher energy than excitonic peak is not simulated.

IV. Performances of CQD photodiodes

To illustrate what these different theoretical performances represent in terms of quantum efficiency for photodiodes, we simulated a simple stack of vertical photodiodes using the transfer matrix method and the n and k indexes previously calculated. Figures 4a and 4b show the results of the optimization of the QDs thin film thickness at different wavelengths for PbS and InAs QDs, the QDs' diameter being each time adjusted so that its excitonic peak corresponds to the incident light wavelength. The obtained EQE maps illustrate the need to increase the thickness of the material's layer to improve the photodiode quantum efficiency but also the existence of resonant cavity phenomena, with the presence of local maxima and minima for thin cavity depths.

Finally, we present in Fig.4c the optical performances related to the excitonic peak only for PbS, HgTe and InAs QDs (the other transitions and the high energy absorption not being considered in this reduced model), assuming photodiodes with a 300 nm thick QD layer (polydispersity of 4%, 0.4 nm-long ligands) without anti-reflective coating on top of the photodiodes. This shows that the excitonic peak transition can allow reaching EQE values above 60% at 940 nm with a thin layer of PbS QDs exhibiting a sharp transition and good rejection ratio of solar background for wavelengths above the excitonic peak, and low cross-talk due to the small thickness of the CQD layer. These results illustrate the potential benefits of using CQD photodiodes for active light systems in infrared applications.

V. Conclusion

In this paper, we presented a methodology to simulate the optical properties of QDs thin films and to predict the quantum efficiencies of CQD-based photodiodes using classical optical simulation methods. This study has allowed us to explain the role of different material parameters (QD size, material choice, ligand length, polydispersity, thin film thickness) impacting the performance of thin films. We showed in particular that it is possible to obtain materials with better performances than established III-V technologies by improving the polydispersity and the volume fraction of QDs in thin films, and by favoring materials such as PbS, PbSe, HgTe and InAs for infrared applications. This reduced model thus represents an appealing tool to anticipate technological developments that can be used for standard imaging applications as well as for the development of a model of CQD hyper-spectrometers for example.

References

[1] Efros, A. L.; Brus, L. E. *ACS Nano* **2021**, *15* (4), 6192–6210.
[2] Talapin, D. V.; Steckel, J. *MRS Bulletin* **2013**, *38* (9), 685–691.
[3] Kagan, C. R.; Lifshitz, E.; Sargent, E. H.; Talapin, D. V. *Science* **2016**, *353* (6302).
[4] Carey, G. H.; Abdelhady, A. L.; Ning, Z.; Thon, S. M.; Bakr, O. M.; Sargent, E. H. *Chemical Reviews* **2015**, *115* (23), 12732–12763.
[5] Steckel, J. S. et al *2021 IEEE International Electron Devices Meeting (IEDM)* **2021**.
[6] Georgitzikis, E.; Malinowski, P. E.; Li, Y.; Maes, J.; Hagelsieb, L. M.; Guerrieri, S.; Hens, Z.; Heremans, P.; Cheyns, D. *IEEE Sensors Journal* **2020**, *20* (13), 6841–6848.
[7] Hinds, S.; Klem, E.; Gregory, C.; Hilton, A.; Hames, G.; Violette, K. *Infrared Technology and Applications XLVI* **2020**.
[8] Gréboval, C.; Darson, D.; Parahyba, V.; Alchaar, R.; Abadie, C.; Noguier, V.; Ferré, S.; Izquierdo, E.; Khalili, A.; Prado, Y.; Potet, P.; Lhuillier, E. *Nanoscale* **2022**, *14* (26), 9359–9368.
[9] Nataliia Sukharevska, N.; Bederak, D.; Goossens, M.; Momand, J.; Duim, H.; Dirin, D.;Kovalenko, M.; Kooi, B.; Loi, M.; *ACS Appl. Mater. Interfaces* **2021**, 13 (4), 5195–5207
[10] Luther, J. M.; Law, M.; Song, Q.; Perkins, C. L.; Beard, M. C.; Nozik, A. J. *ACS Nano* **2008**, *2* (2), 271–280.
[11] Guyot-Sionnest, P. *The Journal of Physical Chemistry Letters* **2012**, *3* (9), 1169–1175.
[12] Voznyy, O.; Zhitomirsky, D.; Stadler, P.; Ning, Z.; Hoogland, S.; Sargent, E. H. *ACS Nano* **2012**, *6* (9), 8448–8455.
[13] Brown, P. R.; Kim, D.; Lunt, R. R.; Zhao, N.; Bawendi, M. G.; Grossman, J. C.; Bulović, V. *ACS Nano* **2014**, *8* (6), 5863–5872.
[14] Delerue, C.; Lannoo, M. *Nanostructures: Theory and Modelling*, Springer, **2004**
[15] Weidman, M. C.; Beck, M. E.; Hoffman, R. S.; Prins, F.; Tisdale, W. A. *ACS Nano* **2014**, *8* (6), 6363–6371.
[16] Dement, D. B.; Puri, M.; Ferry, V. E. *The Journal of Physical Chemistry C* **2018**, *122* (37), 21557–21568.
[17] Chehaibou, B.; Izquierdo, E.; Chu, A.; Abadie, C.; Cavallo, M.; Khalili, A.; Dang, T. H.; Gréboval, C.; Xu, X. Z.; Ithurria, S.; Vincent, G.; Gallas, B.; Mugny, G.; Arnaud, A.; Lhuillier, E.; Delerue, C. *Nanoscale* **2022**, *14* (7), 2711–2721.
[18] Baumgardner, W. J.; Whitham, K.; Hanrath, T. *Nano Letters* **2013**, *13* (7), 3225–3231.

Custom CMOS Image Sensor for Use in an Extreme Low Light Level Electron Bombarded CIS

Verle Aebi*, Kenneth Costello, Edward Yin, Kevin Roderick, Emil Wilke, Lidiya Polukhina, Bruce True, Selim Bencuya, and Rudolph Benz
EOTech, LLC., 3580 Bassett Street, Santa Clara, CA 95054 USA

Steve Huang, Daniel Van Blerkom, Loc Truong, Sam Bagwell, Wilson Law, and Tim Lu
Forza Silicon (AMETEK Inc.), 2947 Bradley Street, Suite 130, Pasadena, CA 91107 USA

**Corresponding author: verle.aebi@EOTechgov.com, +1-408-210-7038*

Abstract -- EOTech and Forza have developed a Backside Illuminated CIS (BSI-CIS) optimized for use in low light level imaging cameras. The MV3.7 CIS has a 9.1 µm pixel, 1920 x 1920 pixel format, 160 Hz frame rate, and 16 bit dynamic range based on a LOFIC pixel architecture. This BSI-CIS has been incorporated as the electron bombarded anode in the ISIE19 Electron Bombarded Active Pixel Sensor (EBAPS®) for use in low light level cameras. The ISIE19 EBAPS is the most recent member of the EOTech EBAPS product family, beginning in 2004. CIS architecture for the low noise (5e-rms), high frame rate, high dynamic range CIS will be presented for the MV3.7. Results are presented for a GaAs photocathode ISIE19 EBAPS. Data presented includes: electron bombarded gain; single photon detection and low light level high dynamic range imagery. The displayed imagery is optimized with a local tone mapping algorithm to map the high dynamic range, low SNR, imagery onto a lower dynamic range display.

1. Introduction

Extreme low light level imaging has been dominated by image intensifier and EMCCD based cameras. Recent advances in low noise CIS and SPAD imaging arrays are beginning to compete with these older technologies. An alternate technology for low light level imaging is based on use of the low noise Electron Bombarded Semiconductor (EBS) gain process. EOTech (formerly Intevac) has developed the EBAPS low light level image sensor technology for extreme low light level cameras.

EBAPS based cameras target applications where camera size, power and low light level performance are critical. Key requirements include high frame rate operation and high dynamic range with single photon sensitivity with no cooling. These requirements all drive the need for improved low light level imagers.

2. EBAPS Technology

Low light level EBAPS image sensors are based on the use of a GaAs photocathode, derived from image intensifier technology, in proximity focus with a high resolution, BSI-CIS anode (Figure 1).

The high voltage (1 – 2 kV) applied between the photocathode and the anode accelerates the emitted photoelectrons to the BSI-CIS anode. Low-noise gain is achieved in the CIS anode by conversion of the high energy photoelectron into electron-hole pairs via the EBS gain process [1] [2] [3]. For silicon an electron-hole pair is generated per 3.64 eV of incident energy. The EBS gain process is deterministic and hence low noise, with a resulting excess noise factor (Kf) of 1.03 [4]. In an EBAPS where the typical operating voltage results in some loss of photoelectrons due to elastic and inelastic backscatter events and incomplete collection of the generated electron cloud the Kf is on the order of 1.2 at 1750V, with temporal noise << 1 photoelectron.

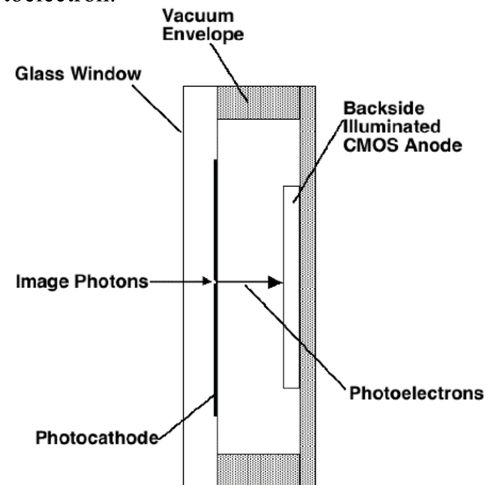

Figure 1. EBAPS Cross Section

The multiplied electrons are collected in the pixel photodiode and are subsequently read out. The EBS gain is high enough to mitigate the pixel readout and dark current noise and other temporal and fixed pattern noise sources, resulting in superior performance at starlight illumination and lower light levels relative to a low noise video frame rate CIS or EMCCD camera. The low noise EBS gain process thus enables a higher signal-to-noise ratio (SNR) at the lowest light levels and single photoelectron detection. The EBS gain process is also a linear gain mechanism as compared to a SPAD and allows signal intensity to be measured.

3. MV3.7 BSI-CIS

Performance of an EBAPS sensor is determined to a large extent by the CIS architecture and design. First, it is essential that the CIS pixel have close to 100% fill factor. Any reduction in fill factor will result in lost photoelectrons. This is equivalent to a reduction in

photocathode quantum efficiency. At the lowest light levels camera performance is dictated by photon statistics. It is essential for the imager to detect the maximum number of photons for good low light level resolution and performance.

Close to 100% fill factor can be achieved in a properly designed BSI-CIS. Frontside illuminated CIS are not used in an electron bombarded mode, both due to lower fill factor relative to a BSI-CIS and because the metal / dielectric stack will block the photoelectrons from reaching the silicon at moderate acceleration voltages (1 - 2 kV). The BSI-CIS silicon surface is passivated to reduce carrier recombination at the surface. A properly designed pixel will allow the generated charge to be collected by the pixel photodiode regardless of photoelectron impact position in the pixel.

Second, the CIS architecture must maximize integration of the image photons with close to 100% temporal duty cycle. This requirement when combined with high fill factor enables the collected signal to be maximized for good low light level performance.

Another critical requirement is high dynamic range to accommodate the intra-scene dynamic range of a nighttime scene with lighting (on the order of 10^5 or 10^6). This results in the capability to better observe scene detail in dark areas of scenes which contain light sources.

Final requirements for a high performance low light level camera include high frame rates (>120 Hz) for use in Augmented Reality (AR) systems, low dark current, megapixel format and large pixel size (~10µm) for increased low light level performance.

The MV3.7 was developed for use in an EBAPS to meet these requirements. The maximum frame rate was increased from 60 Hz for previous generation ISIE11 EBAPS to 160 Hz for the MV3.7 (ISIE19) while CIS noise floor was reduced to improve single photoelectron detection efficiency. The linear dynamic range was increased from 10 bits for the ISIE11 to 16 bits for the MV3.7. The imager format and size was increased to 3.7 megapixel from 2 megapixel for ISIE11.

The MV3.7 is fabricated in a standard 110nm design rule BSI-CIS process. The MV3.7 floorplan is shown in Figure 2. The active image array size consists of a 1920 x 1920 array of 9.117 µm square pixels with additional rows and columns included at the periphery of the array. 66 shielded dark columns are included to enable off-chip row temporal noise correction in the camera Image Signal Processor (ISP). An additional boundary of 15 rows and columns on each side of the active imaging array are included to ensure uniform response in the active image array.

A Lateral Overflow Integrated Capacitor (LOFIC) pixel architecture was chosen for the MV3.7 CIS. The LOFIC architecture enables a high, linear, dynamic range for the CIS. The LOFIC HDR approach retains all charge generated by the photodiode in the overflow capacitor thereby insuring accurate capture of fast transient flashes.

The LOFIC pixel can be used in a standard 4T configuration to enable a low noise Correlated Double Sampling (CDS) readout of the floating diffusion. The pixel incorporates a dual-Transfer Gate (TX) structure to enable charge flow into the overflow (OF) capacitor once the photodiode is saturated. The TXOF voltage is set so charge preferentially flows onto the capacitor and not through the TX onto the floating diffusion. In this mode of operation no charge is lost. At readout the LOFIC pixel is sequentially read, first a “low light level” read is performed to sample the floating diffusion followed by a “high light level read” of the capacitor. Both reads are independently digitized via 11 bit ADCs. The ADCs are column parallel dual 11 bit single slope ADCs for low light and high light data reads from the LOFIC pixel.

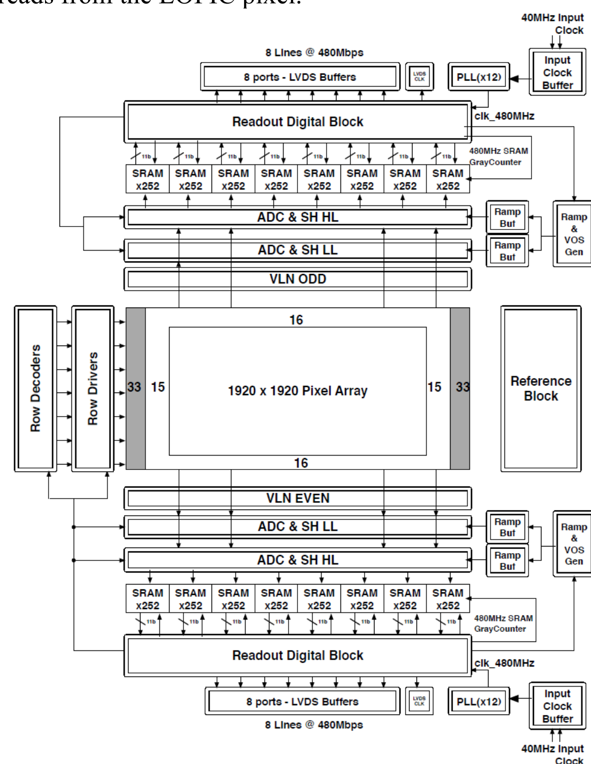

Figure 2: MV3.7 CIS Floor Plan

Both readouts are stored in on-chip SRAM. An on-chip register controlled comparator determines which readout contains useful data. The selected data is read out as a 12 bit word, 11 data bits and 1 flag bit. The flag bit indicates if the data is a low light level read or a high light level read from the capacitor. The camera ISP subsequently converts the data to 16 bits with a linear dynamic range of ~96 dB.

MV3.7 CIS performance values are given in Table 1. The dark current of the pixel at 65°C is higher than desired, but the noise on the dark current is significantly lower than the expected single photoelectron generated signal in the MV3.7 due to the EBS gain. This enables the ISIE19 to remain photocathode dark current limited up to the maximum camera operating temperature.

Parameter	Performance
Pixel Size	9.117 microns
Image Format - CIS	1950 x 1950 pixels
Image Format - EBAPS	1920 x 1920 pixels
Maximum frame rate	160 Hz (Full frame)
Read Noise	5.1 e-
Full Well Capacity (Overflow capacitor)	348,000 e-
Dynamic range	>68,000 or 96dB
Image lag	<1.5 e- average after a saturated frame
Conversion gain – low light level read	64.6 µV/e-
Conversion gain – high light level read	3.0 µV/e-
Pixel Dark Current (65°C)	5286 e-/pix-s

Table 1: MV3.7 CIS performance

4. ISIE19 EBAPS

The ISIE19 uses a GaAs photocathode to achieve low dark current at elevated temperatures [5]. A typical spectral response curve is shown in Figure 3. Emitted dark current is ≤50 fA/cm^2 at 40°C or 0.3 e-/pix-s.

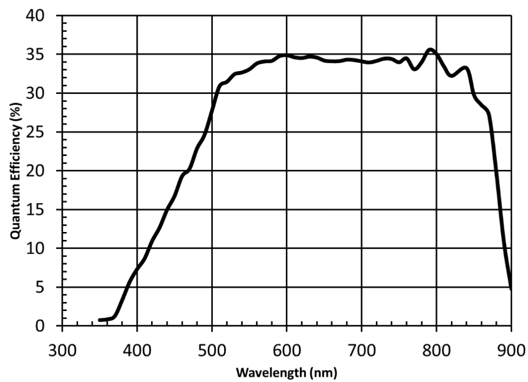

Figure 3: GaAs photocathode Spectral Response

The ISIE19 is operated with 1,750V applied between the photocathode and the CIS anode. The low noise EBS gain process enables a key characteristic of EBAPS: the ability to detect single photoelectrons independent of CIS frame rate. This capability is a function of the ratio of low noise electron bombarded gain to CIS noise floor. Electron bombarded gain increases with voltage applied between the photocathode and the CIS anode.

Figure 4 is a plot of EBS gain versus applied voltage between the photocathode and the electron bombarded MV3.7 anode derived from measurements on several EBAPS. For the ISIE19 the EBS gain is on the order of 300 at the 1,750V operating voltage with the MV3.7 read noise floor on the order 5.1e-. The maximum theoretical EBS gain at 1750 eV incident photoelectron energy is 481 assuming all of the incident energy is dissipated in the silicon with all of the generated electrons collected by the CIS photodiode.

Figure 5 is a series of pulse height distribution curves versus applied voltage between the photocathode and the MV3.7 anode at 120Hz frame rate. As the applied bias voltage is increased, photoelectrons strike the anode with higher energy increasing the number of generated electron-hole pairs (EHP) and the depth into the silicon at which the median EHP is generated. The number of detected electrons (x-axis of figure) was calculated by multiplying the DN value with the responsivity of the analog conversion voltage measured for the MV3.7. The 0 V curve represents the black level of the camera.

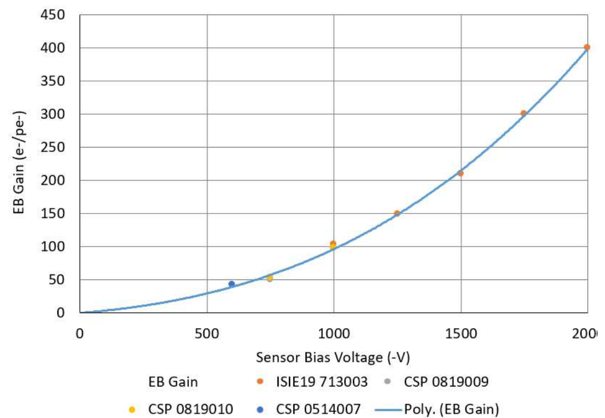

Figure 4: Electron bombarded gain versus voltage

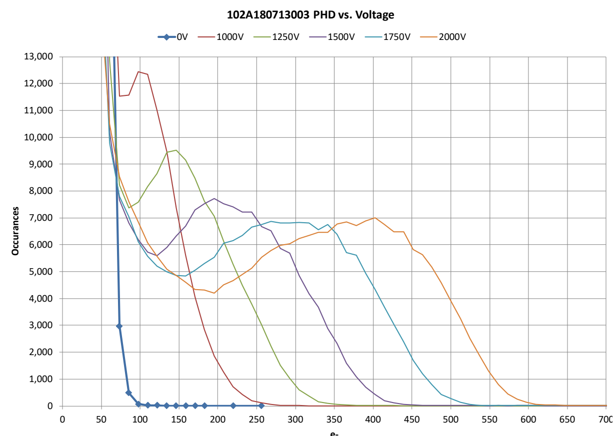

Figure 5: ISIE19 histograms as a function of voltage

At low light levels the LOFIC pixel is in the high sensitivity range. As light level increases the pixel crosses into the high light level range where the MV3.7 read noise is significantly higher, on the order of 100 e-. Cross-over on the LOFIC pixel is determined on a per pixel basis as discussed in Section 3. The cross-over is set at a DN value of ~784DN in the LL channel and ~36DN on the HL channel. At an EBS gain of 300, this equates to ~25 detected photoelectrons with a signal shot noise of ~5 photoelectrons. The signal shot noise after EB gain is well above the input referred read noise of the HL channel. At this cross-over, the HL channel is photoelectron shot noise limited with good SNR.

Figure 6 compares high dynamic range imagery captured with the ISIE19 and the previous generation ISIE11. Both cameras used the same objective lens.

The lens is optimized for low light imaging applications over the GaAs photocathode spectral response range with a 38° horizontal field-of-view for both cameras. The dark corners in the Figure 6 imagery is a result of the lens relative illumination falling off at the ISIE19 and ISIE11 image sensor corners. The ISIE19 was operated at 120 Hz frame rate versus 60 Hz frame rate for the ISIE11 camera. For presentation purposes 12 frames were averaged for the ISIE19 camera and 6 frames for the ISIE11 camera, both representing 1/10th second of imagery. This has been found to result in still images very similar to observation of live video. The scene was challenging as it was to the west an hour after sunset. The high dynamic range of the ISIE19 sensor is evident in the imagery. The ISIE19 ISP contains a Local Tone Mapping algorithm optimized for low SNR low light level imagery to map the camera 16 bit output to 8 bits for display.

Figure 6: HDR scene comparing ISIE19 to ISIE11

5. Chip Scale Packaged (CSP) MV3.7 EBAPS

The primary motivation for the development of the CSP EBAPS is to miniaturize the sensor for those applications that cannot accommodate the physical size of the ISIE19. The CSP eliminates the ceramic package used for ISIE19 and forms the photocathode vacuum seal directly with the MV3.7 chip with the bond pads exterior to the vacuum envelope. The combination of the CSP and electronics will support a 25mm square camera module.

The focus on a small camera size drives multiple trade-space choices. A camera system includes: EBAPS; camera electronics; and a high voltage power supply (HVPS). The size and complexity of the HVPS is driven by the voltage required to bias the EBAPS photocathode. HVPS size can be reduced by minimization of the EBAPS high voltage. Optimal EBAPS performance is achieved when the electron bombarded gain of the photoelectron upon impact with the CIS greatly exceeds the CIS read noise. With a read noise of ~5.1 e- the MV3.7 was a suitable choice for prototype CSP development. At the targeted operation voltage of 750 V the EBS-to-read noise ratio is >10. Figure 7 compares the size of the ISIE19 and CSP sensors.

Figure 7: ISIE19 EBAPS comparison to CSP

6. Conclusion

Low light level cameras are transitioning from image intensifier or EMCCD based cameras to cameras based on low noise CIS, SPAD arrays or EBAPS. This work has developed a 3.7 megapixel, 160 Hz frame rate, high dynamic range LOFIC pixel BSI-CIS optimized for integration with a GaAs photocathode. Single photon detection capability has been demonstrated at 120 Hz frame rate to support AR system needs. Future work includes further development of the CSP and development and testing of new cameras based on the ISIE19 and CSP EBAPS.

References

[1] M. Suyama, A. Kageyama, I. Mizuno, K. Kinoshita, M. Muramatsu and K. Yamamamoto, "An Electron Bombardment CCD Tube," in *SPIE Vol. 3173*, 1997.

[2] V. W. Aebi, K. A. Costello, J. P. Edgecumbe, J. J. Boyle, W. L. Robbins, R. Bell, D. Burt, A. Harris, I. Palmer and P. Pool, "Gallium Arsenide Electron Bombarded CCD Technology," in *SPIE Vol. 3434*, 1998.

[3] V. Aebi and K. Costello, "Electron Bombarded Semiconductor Image Sensors," in *Single Photon Imaging*, vol. 160, Springer Series in Optical Sciences, 2011, pp. 63 - 72.

[4] R. A. LaRue, K. A. Costello, G. A. Davis, J. P. Edgecumbe and V. W. Aebi, "Photon Counting III-V Hybrid Photomultipliers Using Transmission Mode Photocathodes," *IEEE Trans. Electron Devices,* vol. 44, pp. 672 -678, 1997.

[5] K. A. Costello, V. W. Aebi, M. Jurkovic and X. Zeng, "Thermally Assisted Negative Electron Affinity Photocathode". United States of America Patent 10,692,683 B2, 2020.